الجمهورية الجزائرية الديمقراطية الشعبية
وزارة التعليم العالي و البحث العلمي
جامعة وهران للعلوم و التكنولوجيا محمد بوضياف

THESIS

In order to obtain the Doctorate Degree

Presented by : Yamina YAHIA LAHSSENE

Title

Segmentation of medical images by geometric deformable models under topological constraints

Faculty	***: Electrical Engineering***
Department	***: Electronics***
Domain	***: Science and Technology***
Branch	***: Electronics***
Formation Title	***: Electronics***

In front of a Jury composed of :

Jury Members	*Grade*	*Quality*	*Domiciliation*
Abdelhamid LOUKIL	Pr.	President	USTO-MB
Tarik ZOUAGUI	Pr.	Supervisor	USTO-MB
Hadria FIZAZI	Pr.	Reviewer	USTO-MB
Abdelghani GHOMARI	Pr.	Reviewer	Univ. Oran 1
Madani OULD MAMMAR	MCA	Reviewer	Univ. Mostaganem
Mostefa MERAH	MCA	Reviewer	Univ. Mostaganem

Année Universitaire : 2021/2022

تلخيص

تعتبر تجزئة الصور خطوة فعالة في تحليل الصورة الطبية، مثل صور الرنين المغناطيسي، لاكتشاف وتشخيص العديد من الأمراض و/أو التشوهات العضوية وعادة ما يتمّ القيام بذلك يدويا من طرف الخبراء الذين يجدونه متعبا ومستهلكا للوقت. كبديل عن ذلك، تمَّ اقتراح العديد من الأساليب الأوتوماتيكية وشبه الأوتوماتيكية لتجزئة صورالرنين المغناطيسي. الكثير من هذه الطرائق يرتكز على النماذج القابلة للتشوه. نحن أيضا، في هذا العمل، اخترنا تجزئة صورالرنين المغناطيسي باستخدام النماذج القابلة للتشوه الى جانب مقيدات الطوبولوجيا.

افتتحنا اطروحتنا بخلفية نظرية لنوعين من النماذج القابلة للتشويه: المعيارية والهندسية. وركزنا أكثر على النوع الثاني نظرا لتميّزه بإيجابيات عديدة مقارنة بالنوع الاول مثل سلوكه الضمني وسهولة استخدامه وقدرته على التوافق تلقائيا مع التغييرات الطوبولوجية للنموذج. بعدها، قدمنا طريقتين لتقييد مرونة النماذج القابلة للتشويه بكيفية تحفظ الطوبولوجيا الخاصة بها طيلة عملية التجزئة: مبدأ النقطة البسيطة ومبدا قوة المقاومة الذاتية.

بعد ذلك، وصفنا بالتفصيل النموذج القابل للتشويه مع الحفاظ على الطوبولوجيا الخاصة به (TPGDM) الدي اقترحناه لتجزئة صور الرنين المغناطيسي وهو نتيجة دمج ناجح للنموذج المقترح القابل للتشويه مع مبدا القوة ذاتية المقاومة الذي يعمل كمقيد لطوبولوجيا النموذج النشط. احتجنا في البداية لاختبار النموذج دون ثم مع تقييد الطوبولوجيا لغرض اثبات مساهمة هدا الاخير في تحسين نتائج التجزئة. بدانا بتعريف النموذج القابل للتشويه المقترح لتجزئة صور الرنين المغناطيسي والمتمثل في: نموذج مجموعة مستوى ثنائية انتقائية (SBLS) تعتمد على مجموعة مستوى معدلة بمرشح غاوسي ثنائية انتقائية ومعدلة (SBGFRLS) . النموذج SBLS يحقق بنجاح إما تجزئة عامة أو محلية دون الحاجة إلى معدلة ما قبل المعالجة. يمكن لنموذج SBLS، في هيئته المحلية LBLS، أن يتحكم في عدد الاجزاء التي سيتم استخراجها في آن واحد من بين جميع الأجسام الموجودة. ومع ذلك فإن نموذج SBLS لا يمكنه تحقيق المستوى المرجو من الدقة كما قد يؤدي الى استخراج محيطات اشكال غير مرغوب فيها. بعدها اضفنا

مبدا القوة ذاتية المقاومة لنموذج SBLS السابق لتقييد الطوبولوجيا الخاصة به وبهذا توصلنا الى ما اقترحناه كنموذج: مجموعة مستوى معدلة بمرشح غاوسي ثنائية انتقائية ومعدلة ومحافظة على الطوبولوجيا (TPLBLS) وهدا ما ساعد على تحسين اداء النموذج بشكل واضح على عدة مستويات: زيادة في الفعالية رغم نوعية الصورة وعدم استخراج محيطات الاجزاء الغير متوقعة. ايضا النموذج TPLBLS لا يحتاج الى معدلة ما قبل المعالجة وهو قادر على القيام بتجزئة عامة (TPGBLS: مجموعة مستوى معدلة بمرشح غاوسي ثنائية عامة ومعدلة ومحافظة على الطوبولوجيا) وخاصة (TPLBLS: مجموعة مستوى معدلة بمرشح غاوسي ثنائية خاصة ومعدلة ومحافظة على الطوبولوجيا).

ولإثبات صحة المناهج المقترحة للتجزئة أحادية الهدف (بطانة قلب واحدة والورم السحائي) وتجزئة هدفان في ان واحد (بطيني القلب) لاختبار فعالية التجزئة المتزامنة، قمنا باختبار كل من نموذجيناLBLS و TPLBLS على صور للرنين المغناطيسي حقيقية من أربع قواعد بيانات مختلفة للقلب والدماغ؛ استخدمنا عشوائيا 73 شريحة من "RVSC MICCAI 2012" لتجزئة بطين القلب الداخلي الأيمن و176 صورة من "York dataset 2006" لتجزئة بطين القلب الداخلي الأيسرو158 صورة من قاعدة بيانات "Figshare" للدماغ لاستخراج الورم الدماغي (الورم السحائي) وأخيرا 66 صورة للقلب من "MICCAI 2017" لاستخراج بطيني القلب معا وفي آن واحد. قمنا بتقييم نتائج التجزئة التي أسفر عنها كل من نموذج LBLS و TPLBLS ومقارنتها ببعض النماذج الموجودة سابقا باستخدام مقاييس مختلفة: معامل التماثل، ومسافة هوسدورف المعدلة ومعدل الجذر التربيعي للخطأ. تبيّن النتائج التي تم الحصول عليها كفاءة كل من النموذجين المقترحين LBLS وTPLBLS مقارنة ببعض النماذج الموجودة غير أن نموذج TPLBLS يعطي أفضل أداء ويحسن بشكل ملحوظ نتائج التجزئة مما يوفر خطوة أولية أكثر دقة لتحليل الصورة الطبية.

كلمات مفتاحية

تجزئة الصور، النماذج الهندسية القابلة للتشوه، مجموعة مستوى، الحفاظ على الطوبولوجيا، بطينات القلب، أورام المخ.

Abstract

Image segmentation has been considered as a vital step in analysis of medical image, such as MRI, to detect and identify several pathologies and/or organ abnormalities. This is usually performed manually by experts who find it tedious and time consuming. As an alternative, different automatic and semi-automatic methods of MRI segmentation have been proposed in the literature. Many of those methods are based on deformable models. We also, by this work, opted for accurate MRI slices segmentation using deformable models in addition to topology constraints.

We initiated our thesis with a theoretical background of both types of the DMs: Parametric deformable models (PDMs) and geometric deformable models (GDMs). We focused more on GDMs due to their several advantages over PDMs such as their intrinsic behavior, ease of implementation and ability to handle automatic topology changes. Then, we presented two topology preserving concepts: simple point and self-repelling force used to constrain the DMs flexibility in a way that preserves its topology during the segmentation process.

After, we describe in detail our proposed topology preserving geometric deformable model (TPGDM) for MRI segmentation. It's the result of successful combination of our proposed GDM with the self-repelling force topology preserving concept. We needed first to test the GDM without then with topology control in order to

demonstrate its contribution in enhancing the results of segmentation. So, we started by introducing the proposed deformable model for MRI segmentation: Selective binary level set (SBLS). It is based on selective binary Gaussian filter level set (SBGFRLS). It successfully provides either global or local segmentations with no requirement of a preprocessing phase. In its local variant, LBLS (local binary level set) is able to control the number of objects to be segmented simultaneously among all the existing ones. Nevertheless SBLS model couldn't achieve the expected level of precision and it may produces unexpected contours eventually. Then we add the self-repelling force concept to the SBLS model to constrain its topology which is in fact our proposed TPGDM: Topology preserving selective binary level set (TPSBLS). This remarkably enhances the performance of the active model in many ways; more robustness towards image quality and absence of undesirable contours. Also, TPSBLS model doesn't need any preprocessing step and it's also able to ensure global (TPGBLS: Topology preserving global binary level set) or local segmentation (TPLBLS: Topology preserving local binary level set).

To validate and compare the proposed approaches for single target segmentation (one heart ventricle and meningioma brain tumor) and two targets (both heart ventricles) simultaneous segmentation, we tested both LBLS and TPLBLS models on real MRI slices from four different cardiac and brain datasets; We randomly used 73 slices from RVSC MICCAI 2012 for the segmentation of the right ventricle endocardium, 176 images from the York dataset 2006 for the segmentation of the left ventricle endocardium, 158 slices from the brain MRI figshare dataset for the brain tumor (meningioma) extraction and finally 66 cardiac MRI from MICCAI 2017. The segmentation results of LBLS and TPLBLS were evaluated and compared to some existing approaches using different metrics: the dice coefficient of similarity, the

modified Hausdorff distance and the root mean square error. The obtained results show the efficiency of both proposed LBLS and TPLBLS models. However, the TPLBLS approach provided the best performance and remarkably improved the results of segmentation.

Key words

Image segmentation, geometric deformable models, level set, topology preservation, heart ventricles, and brain tumors.

Résumé

La segmentation d'image est une étape essentielle de l'analyse d'images médicales, telles que les images par résonnance magnétique (IRM). Elle a pour objectif de détecter et d'identifier plusieurs pathologies et/ou anomalies d'organes. Cette opération est généralement effectuée manuellement par des experts qui la trouvent fastidieuse et lente. Comme alternative, différentes méthodes automatiques et semi-automatiques de segmentation d'IRM ont été proposées dans la littérature. Plusieurs de ces méthodes sont basées sur les modèles déformables (MDs) que nous avons choisi d'étudier dans cette thèse avec des contraintes de topologie.

Nous rappelons d'abord le contexte théorique des MDs avec ces deux catégories : Les modèles déformables paramétriques (MDPs) et les modèles déformables géométriques (MDGs). Nous nous sommes intéressés plus particulièrement aux MDGs en raison de leurs nombreux avantages par rapport aux MDPs, tels que leur comportement intrinsèque, leur facilité d'implémentation et leur capacité à gérer les changements automatiques de topologie. Puis, nous présentons deux concepts de préservation de la topologie : le point simple et la force auto-répulsive utilisés pour contraindre la flexibilité des MDGs de manière à préserver leur topologie durant le processus de segmentation.

Ensuite, nous décrivons en détail le modèle déformable géométrique avec préservation de topologie TPGDM que nous proposons pour la segmentation d'images IRM. Celui-ci est le résultat d'une combinaison d'un MDG avec le concept de force auto-répulsive servant comme contrainte topologique au modèle actif. Nous voulions d'abord tester le MDG sans puis avec le contrôle de la topologie afin de démontrer sa capacité à améliorer les résultats de segmentation. Nous présentons ainsi le modèle déformable proposé pour la segmentation d'IRM: Ensembles de Niveau Binaire Sélectif (SBLS). Il est basé sur un modèle existant SBGFRLS (Ensemble de Niveau Binaire Sélectif Filtré Gaussien). Il fournit avec succès des segmentations globales ou locales sans avoir besoin d'une phase de prétraitement. Dans sa variante locale, LBLS (Ensemble de Niveau Binaire Local) est à même de contrôler le nombre d'objets à segmenter simultanément parmi tous ceux existants. Néanmoins, le modèle SBLS n'a pas pu atteindre le taux de précision souhaité et il peut éventuellement produire des contours imprévus. Ensuite, nous associons le concept de force auto-répulsive au modèle SBLS pour contraindre sa topologie, qui donne en fait notre modèle proposé TPGDM: Ensemble de Niveau Binaire Sélectif avec Préservation de Topologie (TPSBLS). Cela permet d'améliorer remarquablement les performances du modèle actif à plusieurs niveaux : plus de robustesse vis-à-vis de la qualité de l'image et l'absence de contours indésirables. De plus, le modèle TPSBLS n'implique aucune étape de prétraitement et sert également à fournir une segmentation globale ou locale.

Afin de valider les approches proposées pour la segmentation d'un seul objet (un ventricule cardiaque ou une tumeur cérébrale de type méningiome) et la segmentation simultanée de deux objets (les deux ventricules cardiaques), nous avons testé nos modèles SBLS et TPLBLS sur des coupes (IRM) réelles provenant de quatre bases de données différentes cardiaques et cérébrales; Nous avons utilisé 73 images de la base

RVSC MICCAI 2012 pour la segmentation de l'endocarde du ventricule droit, 176 images de la base York 2006 pour la segmentation de l'endocarde du ventricule gauche, 158 coupes d'IRM cérébrales de la base figshare pour l'extraction du méningiome et enfin 66 slices d'IRM cardiaques de la base MICCAI 2017. Les résultats de segmentation de SBLS et TPLBLS ont été évalués et comparés à certaines approches existantes en utilisant trois métriques : le coefficient de similarité (Dice), la distance d'Hausdorff modifiée et l'erreur quadratique moyenne. Les résultats obtenus montrent la robustesse des modèles SBLS et TPLBLS proposés. Cependant, l'approche TPLBLS a fourni les meilleures performances et a remarquablement amélioré les résultats de la segmentation.

Mots clés

Segmentation d'images, modèles déformables géométriques, ensemble de niveau, préservation de la topologie, ventricules cardiaques, tumeurs cérébrales.

Acknowledgements

In the name of Allah, the most gracious, the most merciful. All thanks to Allah, the lord of both worlds, for being my support and for giving me the will and the courage to overcome all the difficulties, and to complete this work.

My special and deep gratitude to Mr. ZOUAGUI TARIK, Professor at the University of Science and Technology of Oran, for accepting to guide me during this thesis. I thank him for the precious advices, comments he gave me. It is with his supervision and encouragements that this work came into existence.

I warmly thank Mr. MEKKAKIA MAAZA Nasreddine, Professor and Director of the Microsystems and Embedded Systems Laboratory - University of Science and Technology of Oran, for his help and support.

I address my deep thanks and recognition to the members of the jury: Mr. BOUGHNAMI Nabil, Professor at the University of Science and Technology of Oran as the president of jury, Mrs. FIZAZI Hadria, Professor at the University of Science and Technology of Oran, Mr. GHOMARI Abdelghani, Professor at the University of Oran 1, Mr. OULD MAMMAR Madani and Mr. MERAH Mostefa, Lecturers at the University Abdelhamid Ibn Bad of Mostaganem who were kind enough to accept to judge my work as members of the jury.

Finally, my thanks go to all those who, from near or far, contributed to the accomplishment of this modest work, and who could not be mentioned here: family, professors, friends and colleagues.

Table of contents

List of figures

1.5775 , (v)) DC= 54.4517, (w) DC= 94.9314 , (x) μ=5, DC= 97.1878. Initial contours are in red. Obtained contours are in green.

List of tables

List of abbreviations

MRI Magnetic Resonance Imaging

DMs Deformable models

PDMs Parametric Deformable Models

GDMs Geometric Deformable Models

GAC Geodesic Active Contour

CV Chan-Vese

DMT Discrete Morse theory

1D One-dimensional

2D Two-dimensional

AL Adversarial learning

GAN Generative adversarial networks

TGDM Topology-preserving geometric deformable model

ACM Active contour model

SBGFRLS Selective Binary and Gaussian Filtering Regularized Level Set

LBGFRLS Local variant

GBGFRLS Global variant

SPF Signed Pressure Force

SDF Signed Distance Function

SBLS Selective Binary Level Set

GBLS Global Binary Level Set

LBLS Local variant

TPSBLS Topology Preserving Selective Binary Level Set

RVSC Right Ventricle Segmentation Challenge

CT Computed tomography

NMR Nuclear magnetic resonance

T Tesla

SI Signal intensity

T1W T1-weighted

T2W T2-weighted

PD Proton density

STIR Short T1 inversion recovery

FST2W Fat suppression with T2 weighting

BOLD Blood Oxygenation Level Dependent

B0 the static magnetic field

3D three-dimensional

EGDMs Edge-based geometric deformable models

RGDMs Region-based geometric deformable models

ESF edge stopping function

MSM Mumford Shah model

PCM Piecewise constant model

PSM Piecewise smooth model

PDEs Partial differential equations

LBFM Local binary fitting model

LIFM Local image fitting model

LFI Local fitted image

QTGDMs Topology preserving geometric deformable model on adaptive quadtree grid

BQGs Balanced quadtree grids

BOGs Balanced octree grid

SRF Self-repelling force

GT Ground truth

ROI Region Of Interest

DC Dice Coefficient

RMSE Root Mean Square Error

MHD Modified Hausdorff Distance

HD Hausdorff Distance

Chapter I

Introduction

1.1 Context and problem statement

The recent advances in medical imaging technologies have led to providing large amounts of data with an increasingly high level of quality such as Magnetic resonance imaging.

It represents an accurate noninvasive imaging modality. It has proven to be more sensitive and capable of revealing organ abnormalities early on that may not be detected or that are poorly distinguished using other imaging modalities.

Consequently, this increases and encourages the noninvasive analyzing and studying of human organs anatomy and function.

MRI segmentation is one of the important and widely applied tasks in the purpose of medical image analysis.

Indeed, it is commonly implemented as a primary stage for any clinical application involving the detection, and measurement of specific objects for the purpose of medical state recognition and diagnosis. Therefore, the role of segmentation task is crucial in most high-level image processing, any failure in the segmentation process

leads to the failure of the entire analysis outcome including classification or development tracking of specific anatomical regions.

The segmentation of the large and complex MRI datasets is usually performed manually by experts. This process is often tedious, time-consuming and can be prone to differences from one expert to another, not to mention the huge number of slices to be treated.

These difficulties in MRI data segmentation have motivated many researchers to develop various computerized segmentation techniques of different accuracy and degree of complexity in order to assist doctors in qualitative diagnosis by dealing with large datasets, while achieving the accuracy of manual segmentation.

However, MRI segmentation remains a complicated task even for a computer due to the nature of MRI slices and to its quality variation, not to mention the huge variability of the very same medical object properties such as the shape.

Indeed, the low contrast between different anatomical structures or even worse, when different structures have similar appearances in the same image can cause considerable difficulties. On top of that, the image quality is often corrupted by many kinds of noise and artifacts introduced during the acquisition process.

Practically, these difficulties in MRI data segmentation are the main cause of the failure of many classical segmentation models. To this end many researchers have been motivated to develop other computerized segmentation techniques of different accuracy and degree of complexity in order to overcome those challenges and to assist doctors in qualitative diagnosis by dealing with large datasets, while achieving the accuracy of manual segmentation.

1.3 Research hypotheses and objectives

Image segmentation is commonly defined as the subdivision of an image into non-overlapping regions that are homogeneous and meaningful (Lucchese and Mitra, 2001) [1] with respect to some visual feature, such as color or texture [2]. It can be described also as a process of grouping together pixels that have similar properties.

Traditional Image segmentation techniques are generally based on one of two basic properties of pixel intensity values: discontinuity and similarity such as thresholding, edge-based segmentation, region growing segmentation and matching in some cases, those traditional techniques of segmentation can be properly applied. However, for medical imaging, a reliable and accurate segmentation is, in general, very difficult to achieve by purely automatic means, due to poor image contrast, noise, diffuse organ/tissue boundaries, and artifacts. These problems can cause considerable difficulties when applying traditional segmentation techniques.

Thus, a variety of approaches have been computerized to automate and speed up the segmentation process. These approaches include two major branches of methods: registration-based methods [3]–[9] and deformable models (DMs) [10], [11].

The central idea of the former branch image registration for the segmentation is to get prior knowledge on the target image before the process of segmentation. Among widely used registration-based techniques are atlas-based methods, as in the work by Ou et al. [3] and Sun et al. [4], the U-Net approach which was applied by Ronneberger et al. [7] then by He et al. [8]. These registration-based techniques consist in matching the image being segmented with a template [3], [4], [7], [8] as a prior knowledge of the target generated from a sufficient training data set created by experts. More specifically this template can be a shape model of the target as in the

work of Grosgeorge et al. [9] constructed based on a training set of manually segmented shapes. The main drawbacks of these approaches are: The requirement for large manually segmented training sets; the high dependence of the results on the specific choice of a training set and the accuracy of the registration step. Moreover, since anatomical variability in the target may be significant from one subject to another they tend to fail in the case of abnormalities.

On the other hand, Deformable Models (DMs), also known as active contours or surfaces, have been proven to be powerful segmentation techniques and are widely used for medical image segmentation, with no training phase and with interesting results reported by authors such as He et al. [10] or Heimann and Meinzer [11]. Depending on the method of representation and implementation used, they can be explicit, and are known as Parametric Deformable Models (PDMs) as in the work of Cohen [12], Cootes et al.[13], and Xu and Prince [14], or implicit, and are referred to as Geometric Deformable Models (GDMs), in which only the geometric properties of the model are considered to describe deformations of the moving curve or surface [15], [16].

Several researchers have applied DMs for medical image segmentation, for example; Khotanlou et al.[17], [18] and more recently, Babu et al. [19] to extract brain tumors, Avendi et al.[20], [21], Nambakhsh et al. [22] and Bhan [23] to segment a single ventricle of the heart (right or left) or both ventricles of the heart simultaneously as in the work of Arrieta et al. [24], Montillo et al.[25] and Soomro et al. [26].

According to Han et al.[27], GDMs offer several advantages over PDMs due to their intrinsic behavior, ease of implementation and ability to handle automatic topology changes. Some of the existing GDMs, known as edge based GDMs, are based only on

image gradient information. Authors like Caselles et al.[28], Kichenassamy et al.[29] next to Forcadel and Le Guyader [30] introduced their edge based GDM as Geodesic Active Contour (GAC). This class of GDMs becomes ineffective in the case of images with noise and low contrast such as medical images of the heart ventricle as well the brain. Region-based GDMs, in contrast, such as the Chan-Vese (CV) model [31] and its derivatives (Duan et al. [32], Almhdie et al. [33]) rely on region information: instead of detecting high gradients, they search for homogeneous intensity values.

In medical images, the topology of the target to be segmented is known beforehand and many authors find it beneficial to guide their models of segmentation using different concepts to ensure better segmentation of the target since its topology can be already predicted.

Different concepts have been proposed in the literature like topology-aware segmentation methods such as [34] where they proposed a new approach to train deep image segmentation networks robust even near topologically challenging locations (such as weak spots of connections and membranes). It's based on leveraging the power of discrete Morse theory (DMT) to identify global structures including one-dimensional (1D) skeletons and two-dimensional (2D) patches. V. Subeesh et al. presented in [35] an explicit approach that relies on adversarial learning (AL) for topology-aware road segmentation. They used the training methodology of generative adversarial networks (GAN) to reduce topological discrepancies between the probability maps produced by their segmentation network and that of real road networks. Their main contribution is a novel AL strategy for improving connectivity constraints on the output of road segmentation networks. We can cite also the work in [36] where authors used a localized topology-aware edge detection method to enhance

the morphological segmentation of microscopic fossils. They showed significant improvement on morphological segmentation of foraminifera when considering region-based and topology-based metrics. Other researchers [37] proposed to include cylindrical topological constraint, based on persistent homology, applied during network training while addressing the property of variable topologies of the small bowel to generate a topologically correct segmentation of the target. In [38], S. Shit et al. proposed a computationally efficient, differentiable loss function (soft-clDice) for training arbitrary neural segmentation networks. They introduced a similarity measure termed centerlineDice (short clDice), which is calculated on the intersection of the segmentation masks and their (morphological) skeletal in order to guarantee the preservation of topology. All those topology aware segmentation models, mentioned above, are efficient however they require and depend strongly on an appropriate training step. Unlike other techniques where the priory known topology is included with no training phase required. For example, authors who used GDMs proposed to exploit the topology of the target as a term of prior knowledge through a concept that constrains the topology of the active contour and to prevent it from undesirable shrinking or merging. Among these, a topology preserving concept based on pixel information, called the simple point, was introduced in the work of Han et al. [27] to constraint the GAC model [28] in their topology-preserving geometric deformable model (TGDM) and was subsequently employed by Bai et al. [39]. However, according to [40], in many applications, combining this kind of topology-preserving with the level set method is considered to be too restrictive; the primary concern is topological defects such as handles, which are difficult to retrospectively correct. Le Guyader and Vese [41] also stress the arbitrariness of the result produced by the algorithm, depending on the order in which points are treated in the narrow band.

Schaeffer et al. [42] and Duggan [43] combined their active contour model (ACM) with a concept introduced by Le Guyader and Vese [41] known as the self-repelling force concept, to preserve its topology.

In this work, our objective is to propose an efficient method for the segmentation of substances in MRI slices such as heart ventricles and brain tumors. To address this issue, we drew on the geometric deformable model proposed by Zhang et al. [44]. This model is known as the Selective Binary and Gaussian Filtering Regularized Level Set (SBGFRLS). It is a Selective segmentation model that enables one contour to be extracted in its Local variant (LBGFRLS) or all existing contours simultaneously in its global variant (GBGFRLS). This model has several advantages for our purposes: (i) SBGFRLS [44] selectively penalizes the level set function to be binary after each iteration of the process, which avoids accumulating several level set functions; (ii) it uses a new region-based Signed Pressure Force (SPF) that can efficiently stop the contours at weak or blurred edges, which is especially interesting in our case; (iii) the exterior and interior boundaries can be automatically detected with the initial contour being anywhere in the image; (iv) the level set function can be easily initialized with a binary function, which is more efficient to construct than the widely used Signed Distance Function (SDF) used in the CV model [31]–[33]; (v) the computational cost for traditional re-initialization can also be reduced.

In this study, we propose a new approach called Selective Binary Level Set (SBLS) [45], which contrarily to Zhang et al. [44], preserves the details of the image that are necessary for the next steps while reducing the computational cost especially in the segmentation of high resolution images. The proposed approach can be implemented as a Global Binary Level Set (GBLS) [45] designed to extract all existing objects with one initial contour, while its local variant (LBLS) [45] helps to segment either a single

or numerous objects simultaneously using as many initial contours as needed. Therefore, LBLS [45] may be suitable for the segmentation of two contours (right and left ventricles of the heart for example) simultaneously, similarly to the model presented by Arrieta et al. [24] and Budai et al. [46].

Finally, the SBLS [45] is combined with the self-repelling force concept of Le Guyader and Vese [41] to control the topology of the active contour in a way that is neither dominant nor inefficient, while maintaining the other advantages of GDMs. The resulting model is called Topology Preserving Selective Binary Level Set (TPSBLS) [45].

Both proposed segmentation approaches; SBLS and TPSBLS [45] were tested for two clinical applications; Heart ventricle and brain tumor segmentation in real MRI slices provided with their manual segmentations by the dataset of the 15th International Conference on Medical Image Computing and Computer Assisted Intervention (MICCAI) 2012 [47] for the Right Ventricle Segmentation Challenge (RVSC), the Cardiac MRI of the York dataset 2006 [48] for left ventricle segmentations, MICCAI 2017 [49] database of the Automatic Cardiac Diagnosis Challenge (ACDC) workshop held in conjunction with the 20th Conference MICCAI in 2017 for simultaneous segmentation of both heart ventricles and figshare dataset [50] for brain tumor extraction respectively. The proposed methods were also compared to existing models cited above such as GAC [28], CV [31], TGDM [27] and SBGFRLS [44] for heart ventricle and brain tumor segmentation in the same slices using the same conditions of initialization.

1.4 Thesis outline

This document is organized as follows. Chapter two presents history, acquisition techniques and some particularities of magnetic resonance imaging. Then, chapter three introduces the literature review of some existed techniques for medical image segmentation where we report some basics reviews and the use of GDMs for segmentation, SBGFRLS [44] next to a topology preserving deformable models [30], [41] discussing both successes and challenges. In the fourth chapter, we explain, in detail, the methodology that we proposed. The next chapter is dedicated to show and discuss our model results on different MRI cardiac and brain databases compared to some existing methods of segmentation. Finally, we conclude with a summary of our work and a discussion of some possible future directions.

Chapter II

Magnetic Resonance Imaging (MRI)

2.1. Introduction

MRI is a noninvasive modality for imaging. It enables the observation of anatomic structures, physiological functions as well as molecular composition of tissues [51]. indeed, MRI has transformed the role of radiology in medicine since its initial applications in structural imaging in the early 1980s and now it encompasses wider areas of functional and molecular imaging [52]. MRI can provide multiplanar and true 3D datasets of subjects in vivo with high spatial resolution of the order of millimeters in the clinical setting and excellent soft tissue contrast without harmful ionizing radiation. Thus, MRI is considered to be crucially outstanding comparing to other techniques such as computed tomography (CT) modality.

2.2. History of Magnetic Resonance Imaging

Clinical MRI is the result of numerous scientific and engineering advances [53]. It's based on nuclear magnetic resonance (NMR) which can be described as an interaction

of certain atomic nuclei in the presence of an external magnetic field when exposed to radiofrequency electromagnetic waves of a specific resonance frequency [54]. Felix Bloch and Edward Purcell successfully introduced the first NMR spectroscopy experiments in 1945 according to [54]. They also shared the Nobel Prize in Physics in 1952 for the finding. Afterwards, they used NMR experiments for chemical and physical analysis of small samples that could be fit into small-bore NMR spectrometers. Next, NMR evolved into a powerful modality for detailed chemical analysis of molecules. In 1972, Paul Lauterbur introduced the idea of applying field gradients in all three dimensions using back-projection methods applied in CT scanning for images generation. After, wide-bore NMR systems were available and capable of imaging living animals and human limbs, along with larger magnets capable of accommodating a human body which aroused the concept of generating images with NMR. The first in vivo image of human anatomy was reported by Peter Mansfield in 1977; it was a cross-sectional image through a finger. The potential diagnostic value of changes in NMR relaxation was suggested by Raymond Damadian and others and further motivated the development of MRI for clinical use. To avoid the undesirable connotations of the word nuclear among the public Nuclear magnetic resonance imaging was renamed magnetic resonance imaging instead. In 2003, a Nobel Prize in Medicine for MRI was shared by Lauterbur and Mansfield [54].

2.3. MRI acquisition techniques

As mentioned above, magnetic resonance imaging (MRI) is based on the principles of NMR [54], a spectroscopic technique used to obtain microscopic chemical and

physical information about molecules. More specifically, MRI is based on the absorption and emission of energy in the radiofrequency range of the electromagnetic spectrum by means of one or some of their biological elements composing the imaged object [55]. Indeed, due to the fact that Hydrogen nuclei have an NMR signal, clinical MRI primarily images the NMR signal from the hydrogen nuclei given its abundance in the human body [55].

In the presence of a magnetic field, protons behave like small bar magnets, with north and south poles. Nevertheless, the magnetic moment of a single proton is extremely small and random. Therefore, applying a constant magnetic field helps to assume a non-random alignment of magnetic moments represented by the free hydrogen nuclei (protons), resulting in the generation of detectable magnetic moment signals in the presence of radiofrequency energy pulses. These signals have the same direction as the external magnetic field and are dependent on the type of tissue and the speed at which the tissue “relaxes” or gives up its movement. Those signals are then mathematically converted into an image. For clinical use of MRI units, the strength of magnetic field that can be applied varies from 0.3 Tesla (T) up to 1.0 T and whole-body scanners with field strengths up to 3 T.

Despite The advantages of MRI over other imaging modalities like absence of ionizing radiation, high soft tissue contrast resolution, and multiplanar imaging capabilities with high-resolution, the time of MRI image acquisition has been a major weakness. To address this issue, newer imaging techniques (parallel imaging), higher field strength systems and faster pulse sequences, have been considered to enhance differences in the signal of various soft tissues. The contrast of the image highly depends on the signal intensity (SI) of different tissues. Tissues that are rich in free protons, such as water and fat, are very responsive to the radiofrequency pulses and

generate a strong signal. However other tissues with fewer free protons, such as cortical bone and air, are less responsive and generate much weaker signal [56].The strength and timing of the radiofrequency pulse, known as an MR sequence, determines different tissue contrasts. Common basic forms of MR sequences include (see Fig. 2. 1):

T1-weighted (T1W) imaging, on which fat appears bright and fluid appears dark.

T2-weighted (T2W) imaging, on which both fat and fluid appear bright.

Proton density (PD) imaging, on which fat appears bright and fluid appears intermediate-SI.

The Manipulation of the MR sequences allows the demonstration of special tissue characteristics. For example, the signal from fat can be made dark using fat suppression techniques. This is very useful in case of musculoskeletal imaging to increase contrast between bright pathologic tissue and fat with T2 weighting. We cite below some of fat suppression techniques:

-Short T1 inversion recovery (STIR) imaging.

-Fat suppression with T2 weighting (FST2W) imaging.

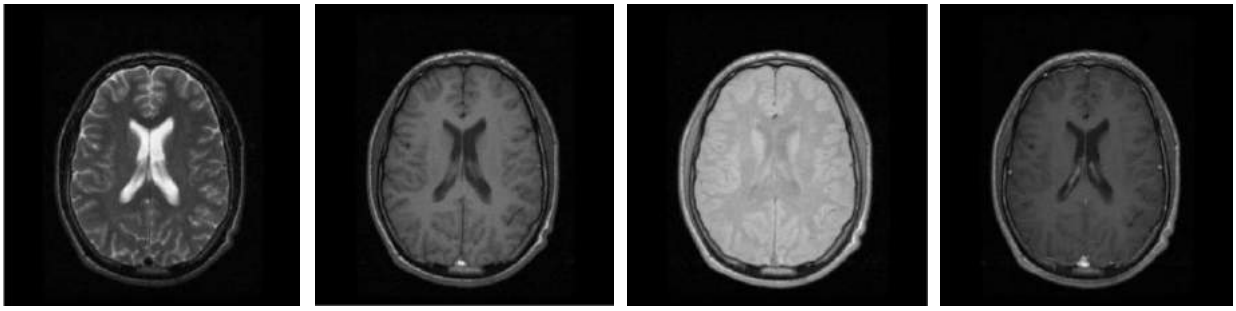

(a) (b) (c) (d)

Fig. 2. 1. Different types of MRI acquisition. The four images are taken from the IBSR database, (a) T1-weighted image, (b) T2-weighted image, (c) a proton density (PD) image, (d) T1 image after Gadolinium injection [57].

2. 4. MRI artifacts

It is not possible to determine a standard definition of an artifact in MRI due to the fact the same artifact that is considered a nuisance to one application can be nothing but a boon to another. For example: the additional signal phase terms generated by blood flow can cause image artifacts, while it also provides an opportunity to measure its phase-sensitive velocity [5]. However, we can describe an artifact as any image component that does not correspond to the object being scanned. MRI artifacts can be caused by scanning system and hardware imperfections, motion and other data inconsistencies. Common kinds of MRI artifacts are cited below:

2. 4. 1. Motion artifacts

This artifact is linked to undesired motions during the examination, either random motions (patient movements, eye movements, swallowing...) or periodic (breathing, heart rhythm...). Movements are a source of image blur and can have a great influence on images (see Fig. 2. 2).

In MRI images, those motions appear as phantom images of the moving structure in different parts of the resultant image. These phantom images may superimpose the structures of interest and therefore lead to disturbance in their grayscale which eventually makes the segmentation process more difficult and inaccurate. This artifact depends on the acquisition phase when undesired motions can occur.

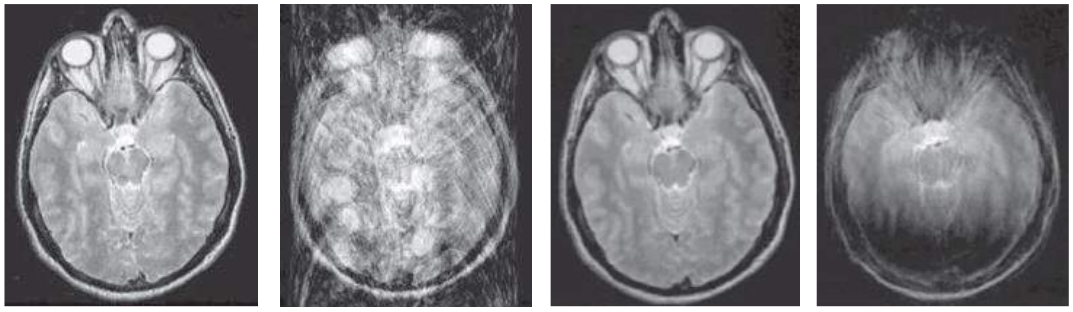

(a) (b) (c) (d)

Fig. 2. 2. Artifacts in brain MRI due to head movement: (a) and (c) **No** motion. (b) and (d) Patient motion [58].

2. 4. 2. Random artifacts

Practically, the data produced by the MRI system can be noisy because of the patient himself due to parasitic emissions caused by thermal agitation of protons and/or the system equipment. The ratio signal to noise is generally calculated to quantify noise disturbance. It represents a function of the observed signal amplitude relative to the noise variation magnitude. To enhance image quality this ratio must be improved by considering different means such as more powerful B0 magnetic field and suitable antennas … Even though this kind of noise can be remarkably reduced in the final reconstructed image, it can't be totally eliminated. Among MRI random noise the Gaussian one is the most common. It usually appears in the Fourier domain of the resultant image, after computing the inverse Fourier transform module. In MRI brain for example the distribution is more like Raleigh in regions of near-zero intensity, such as outside the skull while in regions where it takes a Gaussian distribution otherwise as shown in Fig. 2. 3.

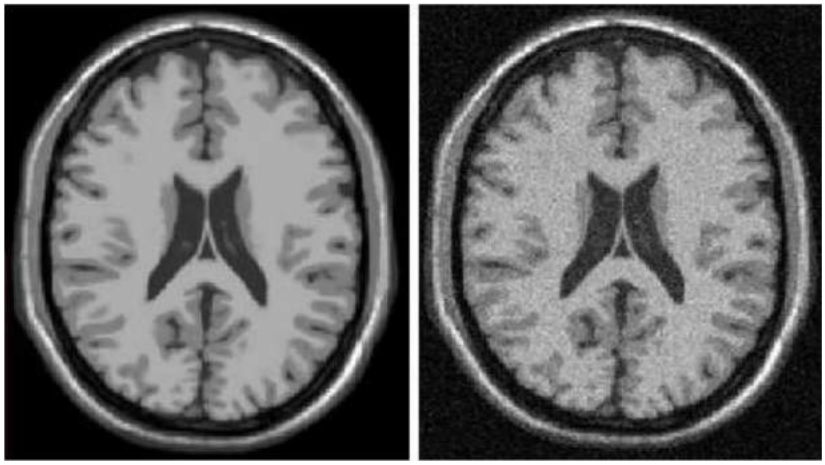

(a) (b)

Fig. 2. 3. MRI with Random noise. (a) MRI image, (b) MRI image with noise: Rice distribution which can be approximated by a Gaussian distribution in regions where the image intensity is not close to zero. Both images are taken from Brainweb Image Base [59].

2. 4. 3. Partial volume

The phenomenon of partial volume (Partial Volume Effect, or PVE in English) is related to the discretization of the space whose voxels are only associated with one gray level, while they represent the data contained in a small volume. Voxels located at the interface between two different tissues contain data of these two tissues, and whose gray level cannot therefore be clearly associated with either of the two classes. such as the interface between the materials (MG, MB, LCR, fat, bone) and in the cortex folds between MG-LCR, as the thickness of the cortical furrows is usually less than the resolution of the images. This phenomenon may also be present in case of blood vessels or fine gray structures in other words when the tissues are too thin to be visible at the image resolution.

2.4. 4 Intensity inhomogeneities

Intensity inhomogeneities represent intensity variations in the same tissue. They are artifacts whose spatial frequency is greater than that of the bias field; we cite two main kinds of them: Inhomogeneities related to practical limitations, imperfections and nonidealities in the hardware of an MRI scanner and those Inhomogeneities related to differences in the histological compositions of the tissues. The first kind produces slow spatial variations in intensity in the reconstructed image, known as a bias field. The most known of their causes is the heterogeneity of the static field B0 static and the excitation field B1 which produces shadow areas in the image caused by the non-uniformity of the magnetic fields produced. Also, the quality and the sensitivity of the receiving antenna used for acquisition. Antennas with spatially stable sensitivity are usually preferred in anatomical MRIs. However, surface antennas are used in fMRI experiments since they provide better sensitivity in a very local area. The reading of the BOLD signal (Blood Oxygenation Level Dependent) is then finer in the region of interest. However, performing an anatomical acquisition without changing the antenna to locate the activated regions on the anatomy leads to anatomical images with a very strong inhomogeneity which makes their automatic processing difficult.

The T1 and T2 relaxation times for both white matter and gray matter tissues depend on age and anatomical regions. Thus, the same gray matter of different structures like the cortex and the basal ganglia such as the putamen can show different intensities on a T1-weighted acquisition. This is due to the fact that the putamen is crossed by a large number of bundles of myelinated fibers which are too thin to be visible on MRI, so the observed intensity results from a mixture of GM and WM due to the partial volume effect. Likewise, WM is lighter in the corpus callosum than in

other regions, because the myelinated fibers in the corpus callosum are more concentrated and oriented in the same direction. Another cause of MRI inhomogeneities is the magnetic susceptibility expressed by the internal magnetization induced by B0 (the static magnetic field) of tissues. Each tissue has a specific magnetic susceptibility. At the interface between two tissues, the difference in magnetic susceptibility causes a disturbance in the B0 field. These local heterogeneities are responsible for localized phase frequency and shifts, causing signal loss, and intensity heterogeneity. They are mainly localized at the air-tissue and cortical bone-tissue interfaces, and very marked in the presence of metallic material. In particular, this artifact is responsible for disturbances due to the mere presence of the patient in the imager.

2.5. Conclusion

As mentioned above artifacts are plentiful in MRI scans. It is necessary to propose suitable and robust segmentation models. The segmentation model can then integrate a constraining term to control the evolution of the segmentation model; however, it shouldn't be too strong otherwise it will lead to a solution guided more by the model than by the observed data. It is essential that the segmentation be as robust and reliable as possible, because too many segmentation errors are likely to confuse the other stages of interpretation in the processing chain, inferring false results. This is the reason why segmentation is generally considered as a crucial step in applications.

In the next chapter, we will present a state of the art of the different deformable models for image segmentation next to topology preserving concepts which can be

combined in order to assure more robustness and precision of the segmentation results.

Chapter III

Literature Review

3.1 Introduction

As mentioned before many authors used registration-based techniques approaches to segment MR slices relying on training phase such as atlas-based methods, as in the work by Ou et al. [3] and Sun et al. [4], the U-Net approach which was applied by Ronneberger et al. [7] then by He et al. [8], Grosgeorge et al. [9] and others ([5], [6]). These registration-based techniques [3]–[7], [9], [60] consist in matching the image being segmented with a template generated from a sufficient training data set created by experts. Therefore, they require large manually segmented training sets and the right choice of a training set.

DMs have been considered as the most active and successful research areas especially in medical image segmentation. They are also known as Active contour or surface models and have been considered as powerful image segmentation since their introduction by Kass et al. [61].

In general, these models [61] may represent curves, surfaces, or higher-dimensional geometric objects, deforming within two-dimensional (2D) or three-dimensional (3D) digital images under both internal and external forces and user defined constraints. Internal forces

rely on the model features itself to preserve the smoothness and the continuity of the model. While external forces, related to the image regions surrounding the active contour, will eventually drive it towards the boundary of the object of interest. By means of energy minimization, the forces will balance out and lead the model to converge to a certain shape.

DMs have been extensively studied and widely used in medical image segmentation with interesting results [10], [11]. Depending on how the model is described. They can be explicit known as PDMs (see [35], [36], [13], [14], [37] and [38] or implicit called GDMs which in turn can be either edge-based (EGDMs) or region-based (RGDMs) (see [65], [15], [30] and [66]–[73]).

In the remainder of this chapter, we will focus on the GDMs and review some of their region-based models. The goal of this chapter is to provide first a theoretical background of the DMs, and then the different formulations proposed based on them illustrated by the following figure (Fig. 3. 1):

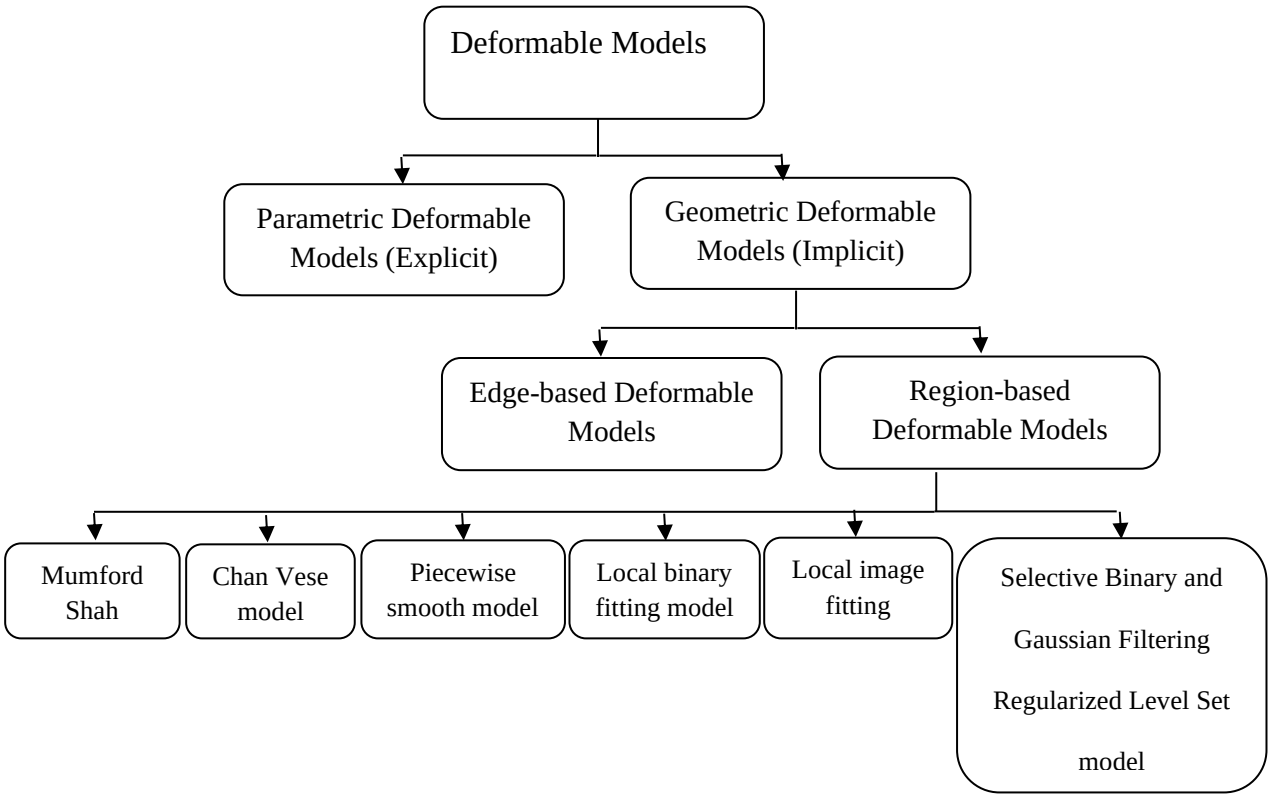

Fig. 3. 1. Review of some variants of deformable models.

3.2 Registration based segmentation approaches

Most of the works based on image registration cited below were applied on cardiac MRI datasets for segmentation purposes as in our case.

3.2.1 Atlas-based segmentation

The term atlas refers to the pair of an anatomical image and a manual labeling [5]. An atlas describes the different structures present in a given type of image Grosgeorge et al. [9].

Atlas-based segmentation uses registration to achieve segmentation. It starts by registering an anatomical image from an atlas with a target image to be segmented. To obtain a segmentation of the target image, the manual labeling of the atlas is transformed using the

mapping determined during the registration; this process is called label propagation [5]. Indeed, atlas-based segmentation approaches make use of intensity and a labeled image that describes the different structures present in a given type of image. Some researchers chose to register a single atlas onto the image to be segmented such as of [6] for the segmentation of heart ventricle. Hence, Several studies have shown that multi-atlas segmentation methods outperform schemes that use only a single atlas, therefore, some authors preferred to use multiple atlases instead like [3], [4]. Ou et al. [3] presented a multi-atlas-registration framework for the segmentation of the Cardiac MR Right. Their central idea is to transfer those expert-segmentations in training images (atlases) onto target images through image registration, and then fuse the transferred segmentations to derive an ultimate segmentation [3].

3.2.2 U-Net based segmentation

The U-Net approach was introduced first by Ronneberger et al. [3] then by He et al. [4] as a convolutional network for biomedical image segmentation. It consists of a contraction path as a left side and expansion path in the right side which is symmetric each one to other in a u-shaped architecture. Therefore it is called U-Net. The central idea of this approach is to train a convolutional network in a sliding-window setup using input images along with their corresponding segmentation maps to predict the class label of each pixel by providing a local region (patch) around that pixel as input. The U-Net output should assign a class label to each pixel including its localization [3].

In the work of Grosgeorge et al. [9] authors introduced a shape template as a prior term constructed from a training set of representative shapes of the target RV obtained by manual segmentation. which is then integrated into the cost function of the well-known graph cut method [74] to guide the segmentation process.

The main drawback of atlas-based methods includes a high computational cost, which is associated with the registration between the target image and multiple atlases, and the dependence of the results on the quality of the atlas set. Both registration and label fusion (for multiple atlases) become quite difficult because of the different structures around the target [3]. The u-net based approach also has some limitations due to its dependence of segmentation results on the quantity and the quality of the training set. Besides, the expense of building a training data set with a manual labeling of medical data while establishing correspondences can also be very challenging.

3.3 Parametric deformable models (PDMs)

Considering a family of closed contours (i.e., curves or surfaces) $C(P,t)$ generated by evolving an initial contour $C_0(P) = C(P,0)$ onto an image, as a result from the front evolution theory [16]. t parameterizes the family and p parameterizes the given contour. The geometric shape of the contour is determined by the normal component of the velocity evolution, while the tangential component determines the parameterization.

The contour C evolves under the velocity field given by a scalar function that often depends on the curvature k of the contour $(C(P,t))$. The contour evolution can be described by the following form:

$$\begin{cases} \dfrac{\partial C(P,t)}{\partial t} = F\big(C(P,t)\big)\vec{n}\big(C(P,t)\big) \\ C(P,0) = C_0(P) \end{cases} \tag{3.1}$$

where

C: The active contour,

$\vec{n}(C)$: The inward normal unit vector along the contour $C(P,t)$,

$F(C)$: A scalar function depends on the curvature k of $(C(P,t))$,

The contour can be transformed into a parameterized curve after discretizing $C(P,t)$ into a set of elements or nodes using a numerical approximation to (3.1) in a Lagrangian framework which is called PDM. During deformation, the node positions have to be updated, and element spacing needs to be adjusted in the purpose of avoiding self-intersection, preserving data fidelity and reducing numerical approximation errors. This type of deformable model allows direct interaction with the model and leads to a compact representation for fast real-time implementation. PDMs can represent boundaries at a sub-grid resolution as it is essential in the segmentation of thin structures.

3.4 Geometric deformable models (GDMs)

The contour $C(P,t)$ can be described implicitly in a different mathematical form, known as: GDMs. They were introduced by Caselles et al. [65] and by Malladi et al. [15] based on the front propagation curve evolution theory [16], [75]. They are represented as level sets of higher-dimensional scalar level set functions evolving in an Eulerian fashion [16] developed by Osher and Sethian in [16], [76] where only geometric measures are used to represent curve or surface deformations. $C(P,t)$, given by eq. (3.1), is implicitly represented as the zero level set (the front) of a smooth Lipschitz-continuous scalar function (x,t) which is known as the level set function, as follows:

$$\begin{cases} \varphi(t,x) > 0 \quad for\ x\ inside\ \Gamma, \\ \varphi(t,x) < 0 \quad for\ x\ outside\ \Gamma, \\ \varphi(t,x) = 0 \quad for\ x\ on\ \Gamma(t). \end{cases} \tag{3.2}$$

where

φ: The level set function,

t: Artificial time (iterations),

$x \in R^2$ in 2D and $x \in R^3$ in 3D,

Γ: A bounded open subset of R^2 around the zero level set of φ.

The implicit contour C can be described, instantly, by the following form:

$$C(.,t) = \{x|\varphi(x,t) = 0\} \tag{3.3}$$

To define the level set function, the signed distance function is commonly preferred for its stability in numerical computations. It represents the signed distance d of a point x to the closed surface defined by the active contour (generally $d > 0$ if x is outside and $d < 0$ if it is inside the surface). Authors in [77], [75] proposed a fast marching method to provide an efficient algorithm for constructing the signed distance function from a given initial contour. However, φ will not remain a signed distance function all the time, so the process will need to be reinitialized [78].

The equation of motion for the level set function $\varphi(x,t)$ can be derived by differentiating $\varphi(x,t) = 0$ with respect to *t* and substituting (3.1), which yields to:

$$\begin{cases} \dfrac{\partial\varphi(x,t)}{\partial t} = F(x,t)|\nabla\varphi(x,t)|, \\ \varphi(C_0(P),0) = 0 \end{cases} \tag{3.4}$$

where

φ: The level set function,

∇ : The gradient operator,

$|\nabla\varphi|$: Denotes the norm of φ gradient.

$F(x,t)$: A scalar function that is only defined originally at the contour location and, hence, needs to be extended to the whole computational domain [16], [79], in order that eq. (3.4) will be applied to the whole space.

GDMs, implemented using level set methods, offer several advantages over PDMs due to their intrinsic behavior, parameterization independence, and ease of implementation. Self-intersections of the evolving contour are naturally avoided. However, they are costly

prevented by PDMs [75]. Also, different geometric properties of the evolving contour, like the normal or the curvature, are easily computed from the level set function [75]. Propagating contour can automatically change topology in GDMs (merge or split) without requiring an elaborate mechanism to handle such changes as in PDMs [75], [80].

3. 4. 1 Edge-based geometric deformable models (EGDMs): GAC

To overcome the need for reparameterization, techniques based on curve evolution theory [76], [66] allow for motion based on geometric measures such as unit normal and curvature. To obtain a new length constraint independent of parameterization, Caselles et al. [66] and Kichenassamy et al. [29] simultaneously proposed the implicit Geodesic Active Contour (GAC); one of the most popular edge-based active contour models [66], It utilizes only local information, such as image gradient, to construct an edge stopping function (ESF) that stops the contour evolution on the object boundaries. The model is based on the idea of considering the boundary detection problem of an object of interest as geodesic computation in a Riemannian space, according to a metric $g(x)$ induced by a given image I, the energy functional of which is given by:

$$E(C) = \int_0^1 g\big(|\nabla I(C(q))|\big)|C'(q)|dq \tag{3.5}$$

where

$C(q)$: A differentiable parameterized curve and $C(q) = \big(x(q), y(q)\big), q \in [0,1]$,

g: The edge stopping function usually expressed as a positive, decreasing and regular ESF $g(|\nabla I|)$ such that $limit_{t\to\infty} g(t) = 0$, given by:

$$\begin{cases} g(|\nabla I|) = 1 \,/\, ((1 + \ \llbracket \beta |(|\nabla (G\_\sigma * I)|)| \rrbracket \ \hat{}\ p\,) \\ p = 1 \ or \ 2 \end{cases} \tag{3.6}$$

The role of g is to attract the curve to regions with sharp gradient where pixels for which $g\left(\left|\nabla I\left(C(q)\right)\right|\right)$ (and hence the associated energy potential) is close to zero.

where

$\beta > 0$: A weight parameter to control the sharpness of detected edges,

$(\mathrm{G}_\sigma * \mathrm{I})$: Denotes convolving image I with G_σ a Gaussian of standard deviation σ.

The evolution of an initial contour C_0 can be described using a steepest descent algorithm to minimize the associated functional energy E_{GAC} yields to the following Euler–Lagrange equation:

$$\begin{cases} \dfrac{\partial C(P,t)}{\partial t} = \Big(g\big(C(P,t)\big)k\big(C(P,t)\big) - \nabla g\big(C(P,t)\big).\vec{n}\big(C(P,t)\big)\Big)\vec{n}\big(C(P,t)\big) \\ C(P,0) = C_0(P) \end{cases} \tag{3.7}$$

where

C: A differentiable parameterized curve,

g: The edge stopping function,

k: The curvature of the contour,

∇: The gradient operator,

$\vec{n}(C)$: The inward normal to the curve,

C_0: Initial contour.

In order to reduce the computational time, a constant velocity term α can be added to efficiently improve the propagation speed. α is known as the balloon force (it controls the contour shrinking or expanding). Thus the previous equation becomes as follow:

$$\begin{cases} \dfrac{\partial C(P,t)}{\partial t} = \Big(g\big(C(P,t)\big)(k\big(C(P,t)\big) + \alpha) - \nabla g\big(C(P,t)\big).\vec{n}\big(C(P,t)\big)\Big)\vec{n}\big(C(P,t)\big) \\ C(P,0) = C_0(P) \end{cases} \tag{3.8}$$

This GAC model can be readily cast within the level set framework. This yields to an equivalent contour evolution process implemented using the following level set function evolution equation:

$$\frac{\partial \varphi(x,t)}{\partial t} = g(x)|\nabla\varphi(x,t)|\left(div\left(\frac{\nabla\varphi(x,t)}{|\nabla\varphi(x,t)|}\right)+\alpha\right)+\nabla g(x).\nabla\varphi(x,t) \qquad (3.9)$$
$$= g(x)|\nabla\varphi(x,t)|(k(x,t)+\alpha)+\nabla g(x).\nabla\varphi(x,t)$$

Despite the importance of edge-based models (GAC) in the segmentation domain, we can cite some of its weaknesses [58], [59] such as poor boundary information due to occlusion, low signal to noise ratio and weak edges.

It is based on edge detection, to segment the image, which relies on gradient information to locate jumps. However, in several cases especially when it comes to real images, such as medical ones, that local information can be unreliable due to the presence of noise and boundaries represented by low gradient [81], [82]. The model has local segmentation property, it can only segment an object if it's surrounded by the initial contour, so it's relevant to set the initial contour properly (GAC can only segment the desired object with a proper initial contour). Also in digital images the discrete gradients are bounded and then the edge stopping function (ESF in Eq. (3.7)) will never achieve zero on edges.

Some EGDMs introduce a balloon force term to overcome some GAC inconvenients, however, it's not easy to be designed. It will force the contour to pass through the weak edge of the object if it's too large. In the opposite case, the contour may not pass through the narrow part of the object.

3. 4. 2 Region-based geometric deformable models (RGDMs)

RGDMs were introduced as a solution to overcome the weaknesses of the GDMs based only on edge information (GAC). It was designed to detect objects whose boundaries are not necessarily defined by sharp gradients; in fact, it ignores edges completely, and the initial contour positioning can be chosen freely in the image, as for the interior contours which can be automatically detected. The principal idea is to subdivide the image into two or more regions of homogeneous intensity values. The process minimizes an energy functional Eq. (3.10) which is used to describe the active contour C during the process. The global form of the energy functional used in RGDMs is given by [31].

$$E(C) = \mu.Length(C) + v.Area(C) + \lambda_1 \int_C |I(x,y) - \overline{I_C}|^2 dx\, dy \qquad (3.10)$$

$$+ \lambda_2 \int_{\Omega/C} |I(x,y) - \overline{I_{\Omega/C}}|^2 dx\, dy \qquad (10)$$

where

E: Energy describing the active contour C,

μ, v, λ_1, λ_2: Positive parameters,

I: The intensity value of the image to be segmented,

$\bar{I}$: The average value of I.

Ω: Image domain,

The third and the fourth term are, respectively, the variance of the intensity level (The homogeneity) inside and outside the contour C.

Each one of the four terms is weighted in order to adjust the influence of each one of them on the total energy, so that, the smaller is the weight, the more the term can increase without penalizing the minimization. Among existing GDMs based on region information we cite the following:

3. 4. 2. 1 The Mumford Shah model (MSM)

David Mumford and Jayant Shah proposed, in [84] a model for image segmentation. They have introduced an energy minimization problem formulated so it allows computing optimal approximations *u* (piecewise-smooth or piecewise-constant) of an image *I* to be segmented.

According to Mumford and Shah [83] the image segmentation problem consists in computing a decomposition of image domain $\Omega \subset R^2$ to Ω_i sub-regions such as:

$$\Omega = \Omega_1 \cup \Omega_2 \cup \ldots \cup \Omega_n \cup K \tag{3.11}$$

Ω: Image domain,

Ω_i: Sub-regions of the image,

K: the boundary between different Ω_i.

For which u is smooth (slow intensity variation) within each sub-region Ω_i of Ω, but discontinuous (sharp intensity variation) acrossing most of the boundary *K* between different Ω_i.

In their work [83] the model of segmentation was presented by the energy functional given by:

$$E^{MSM}(u, C) = \int_{\Omega} (u - I)^2 dx + \mu \int_{\Omega/C} |\nabla u|^2 dx + v|C|, \quad x \in \Omega \tag{3.1 2}$$

where

E^{MSM}: The energy functional of MSM,

C: The active contour,

u: Optimal approximation *u* of an image *I* to be segmented,

Ω: Image domain,

$|C|$: The length of C,

$\mu, v \geq 0$: Positive Constant parameters.

∇: The gradient operator,

The unknown set C and the non-convexity of the above energy functional make it difficult to be minimized. Some alternative methods have been proposed to simplify, modify and minimize the above functional, we can cite as an example the paper [84] where authors presented a multiresolution stochastic Level set method for Mumford-Shah image segmentation.

3. 4. 2. 2 The Chan Vese model (CVM)

The CVM [31] is one of the most popular region-based models for image segmentation. Technically, it combines the reduced MSM [84] and level set method. This segmentation problem is solved interchangeably by computing a gradient descent flow and expensively and tediously re-initializing a level set function.

CVM has been successfully used in binary phase segmentation with the assumption that each image region is statistically homogeneous. It was followed by several works [32], based on it, on 2D segmentation such as [85], as well on 3D segmentation like the work of [86].

Let $I: \Omega \rightarrow R$ be an input image and C be closed curve. The energy functional according to Chan and Vese is defined by:

$$E^{CV}(C, c_1, c_2) = \mu . Length(C) + v . Area\big(inside(C)\big) \tag{3.13}$$

$$+ \lambda_1 \int_{inside(C)} |I - c_1|^2 dx + \lambda_2 \int_{outside(C)} |I - c_2|^2 dx \,,$$

$$x \in \Omega$$

where

E^{CV}: The energy functional of MSM,

C: The active contour,

c_1, c_2: Two constants that approximate the image intensities inside and outside the contour C, respectively,

$\mu, v, \lambda_1, \lambda_2$: Positive Constant parameters,

Ω: Image domain,

$I: \Omega \to R$: The original image.

The first term is The Euclidean length, it's used to regularize the contour, the second is the area term, the third and fourth term representing the variance of the intensity level (i.e., the homogeneity) inside and outside C. Each term is weighted by a fixed parameter ($\mu, v \geq 0$, $\lambda_1, \lambda_2 > 0$) in order to determine its influence on the total energy. μ controls the smoothness of zero level set, v increases the propagation speed, $\lambda_1$and λ_2 control the image data driven force inside and outside the contour, respectively.

After minimizing the above energy functional using the steepest descent method [87], and representing the contour C as the zero level set, we obtain the corresponding variational level set formulation as follows:

$$\begin{cases} \frac{\partial \varphi}{\partial t} = \delta(\varphi)\left[\mu\, div\left(\frac{\nabla \varphi}{|\nabla \varphi|}\right) - v - \lambda_1 (I - c_1)^2 + \lambda_2 (I - c_2)^2\right] \\ c_1(\varphi) = \frac{\int_\Omega IH(\varphi) d\Omega}{\int_\Omega H(\varphi) d\Omega},\ c_2(\varphi) = \frac{\int_\Omega I(1-H(\varphi)) d\Omega}{\int_\Omega (1-H(\varphi)) d\Omega} \\ H(z) = \begin{cases} 1, & if\ z > 0 \\ 0, & if\ z < 0 \end{cases} \end{cases} \quad (3.14)$$

where

φ: The level set function,

I: The intensity value of the image to be segmented,

Ω: Image domain,

H: The Heaviside function,

z: A given function,

$\mu, v, \lambda_1, \lambda_2$: Positive Constant parameters,

The data fitting term $(-\lambda_1(I - c_1)^2 + \lambda_2(I - c_2)^2)$ controls the curve evolution, $\lambda_1$and λ_2 govern the tradeoff between the two terms. Obviously, in Eq. (3.14), c_1 and c_2 are related to the global properties of the image contents inside and outside the contour, respectively. However, such global image information is not accurate if the image intensity inside or outside the contour is inhomogeneous.

Usually, $\lambda_1 = \lambda_2$, $v = 0$ and μ is a scaling parameter. It is set to be small enough, so small objects can be extracted. However, for big objects, it needs to be large enough [31].

As pointed in [31], the CVM can automatically detect all of the contours, no matter where the initial contour starts in the image. So we can say that the CVM has the global segmentation property to segment all objects in an image. But, the model does not work well for the images with intensity inhomogeneity. Vese and Chan extended their work in [88] to utilize multiphase level set functions to represent multiple regions. They called it the piecewise constant model (PCM).

3. 4. 2. 3 The piecewise smooth model (PSM)

In the case of images with intensity inhomogeneities, the CVM [31] for segmentation may fail to achieve its purpose. In order to overcome this inconvenience, Vese and Chan proposed in [88] another method that aims at expressing the intensities inside and outside the contour as piecewise smooth functions instead of constants.

The following energy functional becomes:

$$E^{PS}(u^+, u^-, \varphi) = \int_\Omega |u^+ - I|^2 H(\varphi) dx + \int_\Omega |u^- - I|^2 (1 - H(\varphi)) dx \quad (3.15)$$

$$+ \mu \int_\Omega |\nabla u^+|^2 H(\varphi) dx + \mu \int_\Omega |\nabla u^-|^2 (1 - H(\varphi)) dx$$

$$+ \nu \int_\Omega |\nabla H(\varphi)|, \quad x \epsilon \Omega$$

where

μ, ν: Positive constant parameters,

Ω: Image domain,

$I: \Omega \to R$: The original image,

$u^+(x)$ and $u^-(x)$ are smooth functions in the sub-regions defined as $\Omega^+ = \{x \epsilon \Omega: \varphi(x) > 0\}$ and $\Omega^- = \{x \epsilon \Omega: \varphi(x) < 0\}$, respectively. Minimizing the above energy functional yields to the following Euler–Lagrange equations:

$$\begin{cases} \dfrac{\partial \varphi}{\partial t} = \delta(\varphi) \left[\nu \, div\left(\dfrac{\nabla \varphi}{|\nabla \varphi|} \right) - |u^+ - I|^2 - \mu |\nabla u^+|^2 + |u^- - I|^2 + \mu |\nabla u^-|^2 \right] \\ u^+ - I = \mu \Delta u^+ \; in \; \{x \epsilon \Omega |\; \varphi(x; t) > 0\} \\ \dfrac{\partial u^+}{\partial \vec{n}} = 0 \;\; on \; \{x \epsilon \Omega |\; \varphi(x; t) > 0\} \cup \partial \Omega \\ u^- - I = \mu \Delta u^- \; in \; \{x \epsilon \Omega |\; \varphi(x; t) < 0\} \\ \dfrac{\partial u^-}{\partial \vec{n}} = 0 \;\; on \; \{x \epsilon \Omega |\; \varphi(x; t) = 0\} \cup \partial \Omega \end{cases} \quad (3.16)$$

Obviously, $u^+$and u^-must be obtained by solving the two partial differential equations (PDEs) before each iteration, which cause a very expensive computational cost. Moreover, $u^+$and u^- must be extended to the whole image domain, which is difficult to implement and consequently increases even more the computational cost. In summary, the high complexity reduces the application of the PS model in practice.

3. 4. 2. 4. The local binary fitting model (LBFM)

LBFM is able to segment images with intensity inhomogeneities and is much more efficient and accurate than the PSM. Li et al. [90], [91], proposed the LBFM by embedding the local image information. The basic idea is to introduce a kernel function to define the energy functional of LBFM as follows:

$$E^{LBFM}(C, f_1, f_2) \tag{3.17}$$

$$= \lambda_1 \int_{\Omega} \int_{inside(C)} K_\sigma(x-y)|I(y) - f_1(x)|^2 \, dydx$$

$$+ \lambda_2 \int_{\Omega} \int_{outside(C)} K_\sigma(x-y)|I(y) - f_2(x)|^2 \, dydx, \;\; x, y$$

$$\in \Omega$$

where

$\lambda_1, \lambda_2 > 0$: Constant parameters,

Ω: Image domain,

$I: \Omega \rightarrow R^2$: An input image,

K_σ: Gaussian kernel with standard deviation σ,

f_1, f_2: Two smooth functions that approximate the local image intensities inside and outside the contour C, respectively.

In the level set method, $C \subset \Omega$ can be represented by the zero level set of a Lipschitz function: $\Omega \subset R$. Minimizing the energy functional E^{LBF} with respect to, yields to the gradient descent flow given by the following equation:

$$\frac{\partial \varphi}{\partial t} = -\delta_\varepsilon(\varphi)(\lambda_1 e_1 - \lambda_2 e_2) \tag{3.18}$$

In order to obtain stable evolution of the level set function, a distance regularized term in [91] is incorporated into eq. (3.18). Moreover, the Euclidean length term is used to regularize the zero contour of φ.

Finally, the total variational formulation becomes:

$$\frac{\partial \varphi}{\partial t} = \mu\left(\nabla^2\varphi - div\left(\frac{\nabla\varphi}{|\nabla\varphi|}\right)\right) + v\,\delta_\varepsilon(\varphi) div\left(\frac{\nabla\varphi}{|\nabla\varphi|}\right) - \delta_\varepsilon\,(\varphi)(\lambda_1\, e_1 - \lambda_2\, e_2\,) \tag{3.19}$$

where λ_1 and $\lambda_2$weight the two integrals over regions inside and outside the contour. e_1 and e_2 are defined as follows:

$$\begin{cases} e_1(x) = \int_\Omega\, K_\sigma(y-x)|I(x) - f_1(y)|^2\, dy \\ e_2(x) = \int_\Omega\, K_\sigma(y-x)|I(x) - f_2(y)|^2\, dy \end{cases} \tag{3.20}$$

with

$$\begin{cases} f_1(x) = \dfrac{K_\sigma * [H_\varepsilon(\varphi) I(x)]}{K_\sigma * H_\varepsilon(\varphi)} \\ f_2(x) = \dfrac{K_\sigma * [(1 - H_\varepsilon(\varphi)) I(x)]}{K_\sigma * (1 - H_\varepsilon(\varphi))} \end{cases} \tag{3.21}$$

The standard deviation σ of the kernel plays an important role in practical applications. σ can be seen as a scale parameter that controls the region-scalability from small neighborhoods to the whole image domain [90]. The scale parameter should be properly chosen according to the images. A too small σ may cause undesirable result, while a too large σ will cause high computational cost.

In the following equations, the regularized versions of Heaviside function *H* and Dirac function δ are utilized as follows:

$$\begin{cases} H_\varepsilon(z) = \frac{1}{2}\left[1 + \frac{2}{\pi}\arctan\left(\frac{z}{\varepsilon}\right)\right] \\ \delta_\varepsilon(z) = \frac{1}{\pi}\cdot\frac{\varepsilon}{\varepsilon^2 + Z^2}, \quad Z\epsilon R \end{cases} \tag{3.22}$$

The parameter ε affects the profile of $\delta_\epsilon\,(\varphi)$. A larger ε will lead to a broader profile, which will enlarge the capture range but decrease the accuracy in the final contour location.

Obviously, f_1 and f_2 of Eq. (3.21) can be viewed as the weighted averages of the image intensities in a Gaussian window inside and outside the contour, respectively. This is why the LBFM can well handle images with intensity inhomogeneity.

3. 4. 2. 5 Local image fitting model (LIFM)

K. Zhang, et al in [85] introduced an active contour model with local image fitting. First they defined a local fitted image (LFI) by the following function:

$$I^{LFI} = m_1 H_\varepsilon(\varphi) + m_2\big(1 - H_\varepsilon(\varphi)\big) \tag{3.23}$$

where m_1 and m_2 are defined as follows:

$$\begin{cases} m_1 = mean(I\epsilon(\{x\epsilon\Omega|\varphi(x) < 0\} \cap\ W_k(x))) \\ m_2 = mean(I\epsilon(\{x\epsilon\Omega|\varphi(x) > 0\} \cap\ W_k(x))) \end{cases} \tag{3.24}$$

$W_k(x)$ is a rectangular window function, (a truncated Gaussian window or a constant window). The proposed local image fitting energy functional results of minimizing the difference between the fitted image and the original image as follows:

$$E^{LIF}(\varphi) = \frac{1}{2}\int_\Omega\ |I(x) - I^{LFI}(x)|^2\ dx, \qquad x \in \Omega \tag{3.25}$$

Using the calculus of variation and the steepest descent method [87], $E^{LIF}(\varphi)$ can be minimized with respect to φ to get the corresponding gradient descent. The derivation of the associated level set function is given by:

$$\frac{\partial \varphi}{\partial t} = (I - I^{LFI})(m_1 - m_2)\delta_\varepsilon(\varphi) \tag{3.26}$$

where $\delta_\varepsilon(\varphi)$ is the regularized Dirac function defined in Eq. (3.22).

3. 4. 2. 6 Selective Binary and Gaussian Filtering Regularized Level Set (SBGFRLS) model

SBGFRLS was originally implemented using a regularized level set function [44]. It combines the merits of the traditional GAC [28] and CV models [31]–[33], described below by Eq. (3.27). The SBGFRLS model takes the form of the level set function of the GAC model [28] in which the classical ESF is replaced by the SPF [44]. As a property of the SBGFRLS model is its selectivity, it can be exploited either locally (LBGFRLS) to segment one specific contour, or globally (GBGFRLS) to provide all the existing contours simultaneously.

$$\begin{cases} \dfrac{\partial \varphi}{\partial t} = \alpha.\,\mathrm{SPF}((\mathrm{I}(\mathrm{x})) \cdot |\nabla\varphi(\mathrm{x},\mathrm{t})| + \nabla\mathrm{SPF}((\mathrm{I}(\mathrm{x})) \,.\, \nabla\varphi, & \mathrm{x} \in \Omega \\ \mathrm{SPF}\big(\mathrm{I}(\mathrm{x})\big) = \dfrac{\mathrm{I}(\mathrm{x}) - \frac{\mathrm{c}_1 + \mathrm{c}_2}{2}}{\max\left(\left|\mathrm{I}(\mathrm{x}) - \frac{\mathrm{c}_1 + \mathrm{c}_2}{2}\right|\right)} \end{cases} \tag{3.27}$$

where

φ: The level set function,

t: Artificial time (iterations),

α: Constant velocity term,

Ω: Image domain,

SPF is the signed pressure force function [44] that reflects the statistical information of the two regions of the image inside and outside the active contour. I is a given 2D image, Ω a bounded open subset of R^2 around the zero level set of φ, and c_1 and c_2 are the same average intensities, used to minimize the energy function of the CV model [31]–[33], inside and outside the contour, respectively.

The proposed algorithm in [44] can be summarized as follows:

1. Set a contour Ω_0 to initialize the level set function $\varphi(x, t = 0)$ as:

$$\varphi(x, t = 0) = \begin{cases} -1 \text{ for x inside } \Omega_0, \\ 1 \text{ for x outside } \Omega_0, \\ 0 \text{ for x on } \partial\Omega_0. \end{cases} \tag{3.28}$$

2. Compute the SPF according to Eq. (3.27).

3. Compute the level set function $\varphi(x, t)$ using Eq. (3.27) without the second term [44] as follows:

$$\frac{\partial \varphi}{\partial t} = \alpha . \mathrm{SPF}((I(x)) \cdot |\nabla \varphi(x, t)|, \qquad x \in \Omega \tag{3.29}$$

4. Let $\varphi = 1$ for $\varphi > 0$; otherwise, $\varphi = -1$. (This step is selective to ensure the local segmentation property and is necessary to segment specific objects.)

5. Regularize φ using a Gaussian kernel G with a standard deviation σ ($\varphi(x, t) = \varphi(x, t) * G_\sigma$),

6. Stop if $\varphi(x, t)$ has converged, otherwise return to step 2.

3.5 Topology preserving geometric deformable models (TPGDMs)

The ability to automatically change topology is often presented as an advantage of the level set method over explicit deformable models. However, this behavior turns out to be a liability in some applications, where a prior knowledge of the target topology is known. This is typically the case in medical image segmentation, since the topology of the target to be segmented in medical images is known in advance. Therefore many studies using GDMs based on the level set function were designed using a novel topology-preserving level set method, which aims to constrain the flexibility of the GDM in order to control merging or shrinking and ensure topology preservation while maintaining the other advantages of standard GDMs.

This is achieved by combining the GDM with a topology-preserving concept such as simple point [27], [39] or self-repelling force [41]. In the present work, the SBGFRLS [44] as a GDM of segmentation and the topology preserving concept based on self-repelling force [41] were focused on and are introduced in this section.

3.5.1 Topology definition

Topology is a branch of mathematics that studies the properties of geometric figures that are preserved through deformations, twisting and stretching, hence without regard to size, absolute position.

In our case, the topology of an object in a 2D image defines the number of its connected components, i.e. cavities and handles. Preserving an object's topology during the image transformation means that its final form remains homeomorphic to its initial one [40]. By definition, two objects are homeomorphic if there exists a bijective transformation that maps one onto the other and both the transformation and its inverse are continuous (the

transformation is called a homeomorphism) [40]. The question of preserving topology is thus equivalent to finding a transformation that is a homeomorphism [92].

Usually, GDMs inherently allow changes in the topology of the active contour by freely splitting or merging the connected components. However, in our case of medical image segmentation, where the target to be segmented has a predefined shape, it is beneficial (lower computing complexity and cost) for the segmentation process to set an initial contour that is homeomorphic to the target as long as the topology of the evolving contour is constrained by keeping constant the number of connected components defined during the initialization of the GDM. In what follows, we describe two of the existing concepts exploited to preserve the topology of GDMs in the literature: The simple-points based concept introduced by Han et al. [27] and the Self-Repelling Force concept [30], [41].

3.5.2 Topology preserving geometric deformable models using simple point concept for topology constraining

The Simple-points shem was introduced by Han et al. [27]. It was used later in [39] where authors proposed a simple point topology preserving level set by means of a balanced quadtree grids, as a new way of implementation, to maintain computational efficiency and a manageable size contour. More recently, the same previous concept [63] was brought by [93].

The works [27] and [94] of Han *et al.* proposed to preserve the topology of the implicit contour while the embedding level-set function is evolving. Their method has been applied to the GAC model [66].

The key idea of their method to preserve topology lies in the concept of simple point, based on the theory of digital topology. The authors assume that the topology of the zero level set is equivalent to the topology of the digital object boundary. The topology-preservation problem is, therefore, simplified in the following way; the topology of the implicit contour can change

only if the level-set function changes sign at a grid point. This is only a necessary condition: not every change of sign of the level-set function implies a topology change of the zero level set and consequently of the digital object boundary. A grid point of a binary object is simple if it can be added or removed without changing the topology of both the object X and its background $\overline{\mathrm{X}}$, i.e. without changing the number of connected components, cavities and handles of both X and $\overline{\mathrm{X}}$. A simple point is easily characterized by two topological numbers with respect to the digital object X and a consistent connectivity pair $(n, \bar{n})$. These numbers, denoted $T_n(x, X)$ and $T_{\bar{n}}(x, \bar{X})$ (or T_n and $T_{\bar{n}}$), have been introduced by G. Bertrand in [95] as an elegant way to classify the topology type of a given voxel. The values of $T_n(x, X)$ and $T_{\bar{n}}(x, \bar{X})$ characterize isolated, interior and border points as well as different kinds of junctions. In particular, a point is simple if and only if$T_n(x, X) = T_{\bar{n}}(x, \bar{X}) = 1$. Their efficient computation, which only involves the 26-neighborhood, is described in [93].

Thus, Han *et al.* introduce an algorithm that monitors at each iteration, the changes of sign of the level-set function and prevents the level-set function from changing sign on grid points which are not simple. Therefore, the procedure is pixel based. Which means, for more accuracy, the resolution of the underlying computational grid needs to be improved. Consequently, both the computational cost and the size of the resulting contour increase dramatically. In order to maintain computational efficiency and to keep the contour size manageable, Han and Prince [39] have improved their previous topology preserving approach [27] to a topology preserving geometric deformable model on adaptive quadtree grid (QTGDMs). In order to do this, definitions and concepts from digital topology on regular grids were extended to balanced quadtree grids (BQGs) so that characterization of simple point could be made.

DMs on balanced quadtree grids have been introduced, later, in [96] where they represented another implementation of the classical simple point topology preserving GDMs using a balanced octree grid (BOGs) instead of BQGs.

The simple point condition is a very efficient way to detect topological changes during a level set evolution. However, in many applications, the topology-preserving level set method of Han et al. is too restrictive. The primary concern is topological defects such as handles, which are difficult to retrospectively correct [94], [97]–[100]. On the other hand, changes in the number of connected components (including cavities) during the evolution are less problematic.

Ségonne in his works [101]–[103] presented a novel genus preserving level set based on an extended concept of simple point, called multisimple point (genus is a topological invariant representing the number of handles). The proposed framework criterion ensures that no handles are generated or suppressed while splitting or merging the components of the object. (For example, if the initial contour has a spherical topology, it may split into several pieces, generate cavities, go through one or several mergings, and finally produce a specific number of surfaces, all of which are topologically equivalent to a sphere.) .The topological numbers of a point x are locally computed and do not carry any information on the global connectivity of the neighboring connected components of x (they measure the number of connected components in the sets $N_n(x, X)$ and $N_{\bar{n}}(x, \bar{X})$. In order to integrate information on the global connectivity, we consider the set $C_n(x, X)$ of n-connected components of $X\backslash\{x\}$ that are n-adjacent to x. We say that a point is multisimple relative to an object X if and only if it can be added or removed without changing the number of handles and cavities of the object. Contrary to the case of simple point, the addition of a multisimple point may merge several connected components, and its removal may split a component into several parts.

Authors in [104] incorporates a Chan-Vese active contour with topology control (using Euler numbers such as EN and NC: numbers of connected regions of image object) allowing the control of preserving or splitting active contours, these numbers are global attributes of topology and are easier than the simple point concept to control global topology.

However, authors stress the arbitrariness of the result produced by the algorithm based on simple point concept, depending on the order in which points are treated in the narrow band.

3.5.3 Topology preserving geometric deformable models using self-repelling force (SRF) concept for topology constraining

Unlike Simple-Points scheme for topology preservation where topology is tested after each step of the segmentation process, self-repelling force based concept is included into the variational framework. This allows for a more granular and far more "natural" approach to topology preservation. It was introduced first by Le guyader et Vese [41] in their model of segmentation based on an implicit level-set formulation and on the geodesic active contours under topological constraint. Self-Repelling Snakes bases its "repelling" factor on a simple geometric observation.

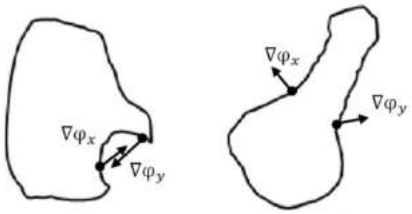

Fig. 3. 2. Geometric observation of a normalized moving front.

Fig. 3. 2 shows how the Self-Repelling Force can be an indicator of topology changes. Considering two neighboring points x and y belonging to the zero level set, C of the signed distance function φ. ∇φ(x) and ∇φ(y) are the unit outward vectors normal to the contour at

these points. According to [30], [41], when the contour is about to merge, split or have a contact point (i.e., when the topology of the evolving contour is about to change), the Euclidean scalar product $\langle\nabla\varphi(x),\nabla\varphi(y)\rangle$ reaches its maximum, thus increasing the topological energy (Etop).

In other words, if the outward normal vectors (fig 1.1) to the level lines passing through points x and y have opposite directions, the inner product term ($-\langle\nabla\varphi(x),\nabla\varphi(y)\rangle$) causes the energy functional to increase sharply (eq. (3.30)), thereby, avoiding breaking or merging of the curve.

$$\begin{cases} -<\vec{n}(x),\vec{n}(y)>\cong 1 & (a) \\ -<\vec{n}(x),\vec{n}(y)>\cong 1 & (b) \\ -<\vec{n}(x),\vec{n}(y)>\cong -1 & (c) \\ -<\vec{n}(x),\vec{n}(y)>\cong 0 & (d) \end{cases} \tag{3.30}$$

Recall that the normal of a level set front is defined by $\frac{\nabla\varphi}{|\nabla\varphi|}$. Approximating φ to a signed distance function yields $|\nabla\varphi| = 1$, which reduces the scalar product from above (eq. (3.30)), to$-\langle\nabla\varphi(x),\nabla\varphi(y)\rangle$.

Le Guyader et al. [41] introduced their geometric information as a variational problem (Eq. (3.30)) to preserve the topology in methods based on level set. The Euclidean scalar product is weighted with an exponential force based on distance in order to decrease the weight of points further away from each other [41].

$$\mathrm{E_{top}}(\varphi) = -\int_{\Omega}\int_{\Omega} \exp\left(-\frac{\|\mathrm{x}-\mathrm{y}\|_2^2}{\mathrm{d}^2}\right) < \nabla\varphi(\mathrm{x}),\nabla\varphi(\mathrm{y}) > \tag{3.31}$$

$$\cdot\, H(\varphi(\mathrm{x})+1)\mathrm{H}\big(1-\varphi(\mathrm{x})\big)\mathrm{H}(\varphi(\mathrm{y})+1)\mathrm{H}\big(1-\varphi(\mathrm{y})\big)\mathrm{dx}\,\mathrm{dy}$$

$$\mathrm{H}(z) = \begin{cases} 1, & if\ z > 0 \\ 0, & if\ z < 0 \end{cases}$$

where

E_{top}: Functional energy [30] for the topology preserving,

φ: The level set function,

Ω: Image domain,

H: The Heaviside function,

z: A given function,

x, y: Two neighboring points determined by the windowing function $\left(\exp\left(-\frac{\|x-y\|_2^2}{d^2}\right)\right)$,

d: The width of the windowing function,

l: The width of the narrow band, $\{x\epsilon\Omega| -l \leq \varphi(x) \geq l\}$, around the zero level curve of φ which denotes the evolving contour.

3.6 Conclusion

DMs are considered one of the popular approaches particularly in medical image segmentation. DMs can evolve according to internal forces and external forces derived from the image characteristics. In this chapter, a detailed overview was provided of different kinds of DMs with particular focus on GDMs. These various techniques are categorized in two groups based on the external force extracted from the image (Edge and region based). The latter group has received a tremendous amount of attention in medical image processing. We also mentioned that different enhancements have been proposed all over the years, including adding terms based on the target's prior knowledge such as shape, size, topology which has got our attention. In the following chapter, we present first, our proposed GDM: Selective binary level set (SBLS) [45] based on the SBGFRLS model [44] then, our Topology preserving selective binary level set (TPSBLS) [45].

Chapter IV

Proposed geometric deformable models for medical image segmentation

4. 1 Introduction

This chapter encompasses the different contributions achieved during the thesis for medical image segmentation of heart ventricle endocardium and brain tumor in real MRI slices. First, we describe our proposed GDM for segmentation known as Selective Binary Level Set (SBLS) [45]. Then, we introduce the proposed Topology Preserving Selective Binary Level Set (TPSBLS) model [45] which is the result of coupling the SBLS model [45] with a topology preserving term based on the self-repelling force concept of Le Guyader and Vese [41]. Examples of segmentation have been presented along this chapter to describe and compare the performances of each approach.

4.2 Selective binary level set (SBLS)

4.2.1 SBLS description

SBLS is based on the SBGFRLS model [44] with no Gaussian smoothing step originally set to regularize the level set function at each phase of the process. This preserves the details of information imported by the model that are necessary for the next steps of the process and reduces the computational cost especially in the segmentation of high resolution images.

The SBLS model can be exploited as a local or global approach for segmentation. The global variant considers all existing objects surrounding the initial contour equally as targets and the process involves the entire image. Unlike the SBGFRLS model [44], the local variant of SBLS [45] processes locally by considering only one or *n* specific targets simultaneously, using one or *n* initial contours, respectively.

4.2.2 SBLS implementation and results

The resulting SBLS segmentation algorithm in its all possible variants is described below in Fig. 4. **1** and summarized in the following steps:

1. Set *n* initial contours Ω_i defined by an initial level set function $\varphi(x, t = 0)$ as:

$$\varphi(x, t = 0) = \begin{cases} -1 \ \text{for x inside} \ \Omega_i, \\ 1 \ \text{for x outside} \ \Omega_i, \\ 0 \ \text{for x on} \ \partial\Omega_i, \\ \Omega = \cup \ \Omega_i, \\ i = 1, .. n \end{cases} \tag{4.1}$$

2. Compute the SPF using Eq. (3.27).

3. Update $\varphi(x, t)$ using SBLS [45] formulation (Eq. (3.29)),

4. If (Local segmentation), set $\varphi(x, t) = 1$ for $\varphi(x, t) > 0$; and $\varphi(x, t) = -1$ otherwise.

Else if (Global segmentation), jump to step 5,

5. Stop if $\varphi(x,t)$ has converged, otherwise return to step 2.

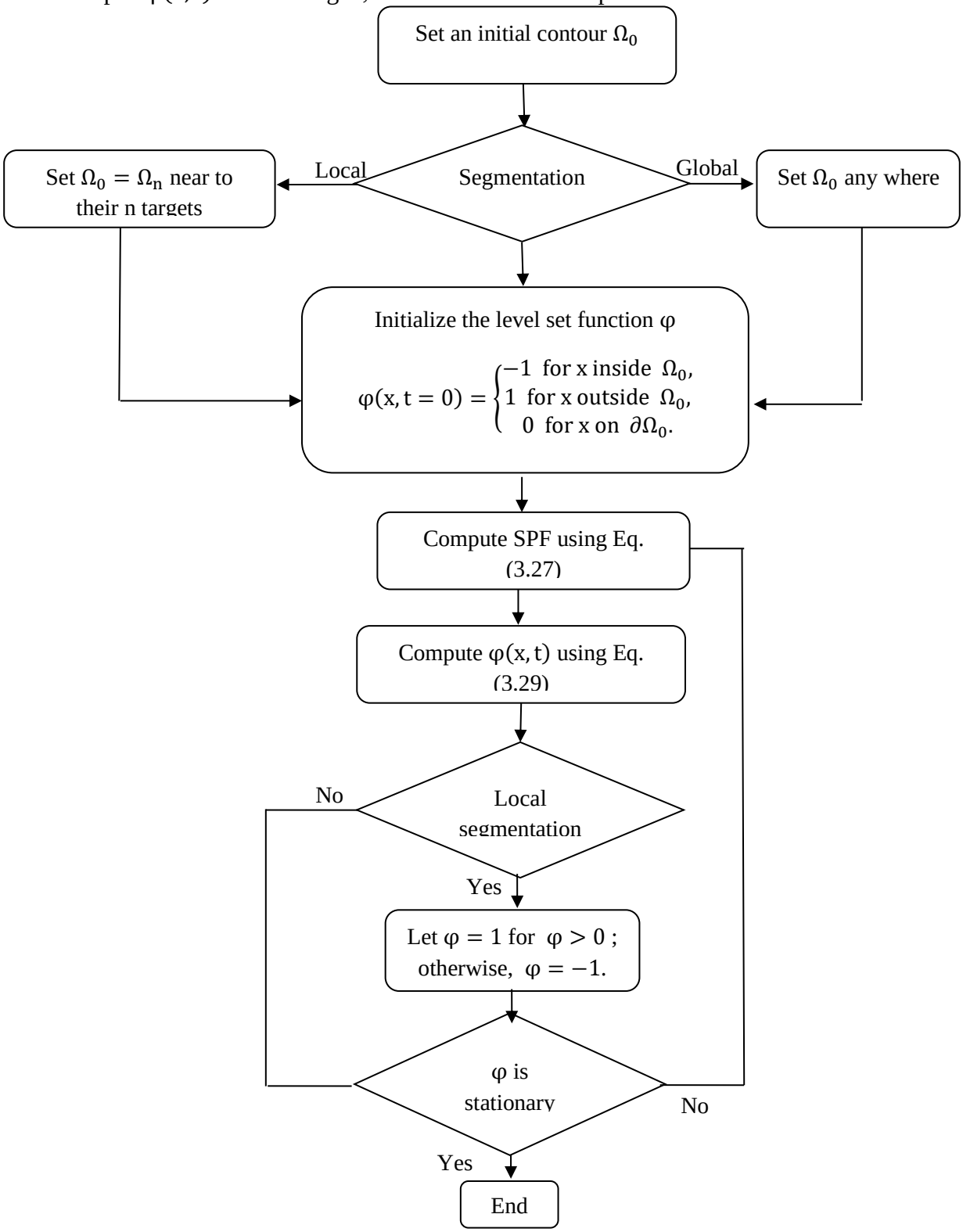

Fig. 4. 1. The algorithm of the proposed Selective Binary Level Set (SBLS) model [45] for segmentation.

Note that in the algorithm, step 4 is a selective step. It is the key step to ensure a local segmentation (LBLS or TPLBLS) [45]. More precisely, it makes the deviation $|\nabla\varphi|$ that is far from the interface of φ close to zero. Thus, only $\varphi(x)$ near to the interface will evolve and this is how the evolution will take local property. Removing step 4 leads to a global segmentation.

The SBLS model [45] presented in Eq. (3.29) is a level set function governed by the parameter α. Its value is relative to the image quality (noisy, smooth, …) and size. More specifically, if the image is relatively noisy and of high resolution, α needs to be high. However, in the case of an image with good quality and small dimensions, choosing high values of α leads to the quick convergence of the SBLS model [45] and possible missing of weak contours. Note that if α is too small, the execution time can be very high and the evolution of the active contour will become stationary or blocked by high gradients in the image.

Hereafter, some results of local segmentation are presented using LBGFRLS [44] and LBLS [45] applied on both synthetic and real images.

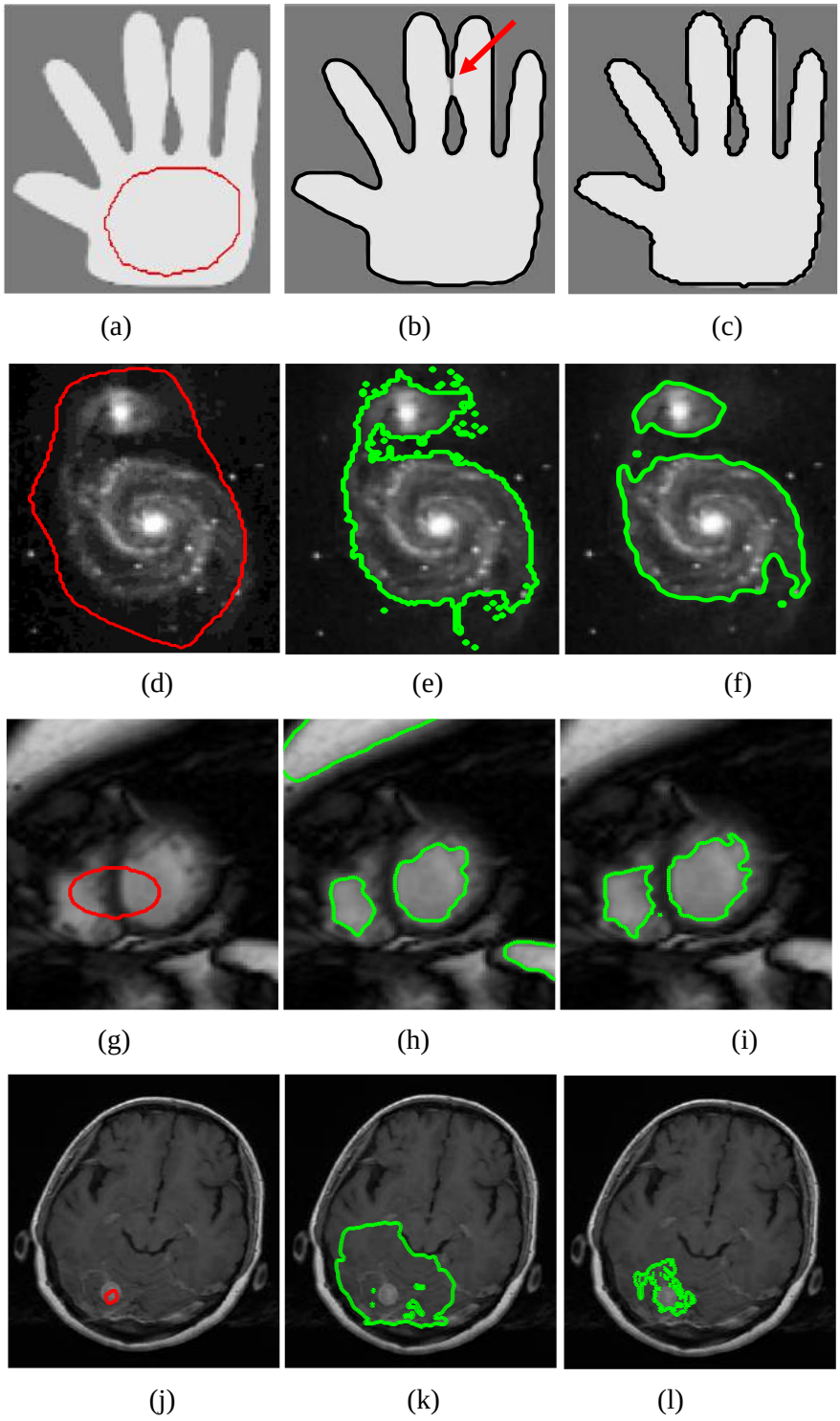

Fig. 4. 2. Segmentation results of LBGFRLS and LBLS [45]. Images with initial contour (a) - hand phantom, (d) - galaxy image, (g) - heart image from MICCAI 2012, and (j) - brain image from figshare dataset. LBGFRLS segmentation results (b), (e), (h) and (k). LBLS [45] segmentation results (c), (f), (i) and (l). $\alpha = 20$ for (a) and (d), $\alpha = 10$ for (g), $\alpha = 20$ for (j). Initial contours are in red. Obtained contours in black and green.

The local segmentation outcomes of a hand phantom image (362x380) presented in the first line of Fig. 4. 2 demonstrate that unlike LBGFRLS [44] (Fig. 4. 2 (b)), using LBLS [45] successfully keeps the boundary of each finger separated, and the final contour correctly reflects the shape of the hand (Fig. 4. 2 (c)). As for the galaxy image, it was supposed to determine one boundary of the galaxy as a single object. Neither LBGFRLS [44] (Fig. 4. 2 (e)) nor LBLS [45] (Fig. 4. 2 (f)) was able to provide the expected segmentation and clearly did not preserve the topology of the initial contour. The same holds for heart ventricle segmentation in a heart image from MICCAI 2012 dataset [47] (see (Fig. 4. 2 (h) and (i)) and for tumor extraction in a brain MRI slice of figshare dataset [50] (see (Fig. 4. 2 (k) and (l)) where both the LBGFRLS [44] and the LBLS models [45] failed to preserve their topologies.

Using the proposed LBLS [45] in its current form may fail to provide a correct segmentation. This is due to the flexibility of the explicit DMs. Consequently, the model allows the initial contour to undergo considerable automatic changes in its topology (shrinking or merging). This affects negatively affects the evolution of the active contour and gives, eventually, a contour with a different topology compared to the initial one and/or undesirable contours as shown in (Fig. 4. 2 (f), (i) and (l).

4. 3 Topology preserving selective binary level set (TPSBLS)

4. 3. 1 TPSBLS description

Even though the automatic changing of topology is a point of strength of GDMs, in the present case of heart ventricle or brain tumor segmentation, it is considered as a limit because the topology of the target can be predefined. It is therefore possible to initialize the active contour to be homeomorphic to the target.This then leads to the challenge of orienting and constraining the automatic changing of the level set in order to maintain the initial topology of the SBLS model [45] during the segmentation process [41]. To this end, we propose to

minimize the functional energy of the SBLS model [45] (E_{GDM}) constrained by E_{top} [41] which is based on the Self-Repelling Force concept [30], [41] in order to preserve the level set (φ) topology as follows (Eq. (4.2)).

$$\min_{\varphi}\left(\mathrm{E_{GDM}}(\varphi)+\mu\mathrm{E_{top}}(\varphi)\right) \tag{4.2}$$

where φ is the level set function, $\mathrm{E_{GDM}}$ is the functional energy of the SBLS model [45], $\mathrm{E_{top}}$ the functional energy [41] for topology preserving, and μ is a positive tuning parameter.

4. 3. 2 TPSBLS implementation and results

The resulting level set (TPSBLS) [45] formulation that minimizes the functional energy of the proposed model defined by Eq. (4.2) is described below:

$$\frac{\partial\varphi}{\partial t}=\alpha.SPF((I(x))\cdot|\nabla\varphi(x,t)|+\frac{4}{d^2}\mu\,H(\varphi(x)+l)H\big(l-\varphi(x)\big) \tag{4.3}$$

$$\int_{\Omega}\left[(x_1-y_1)\frac{\partial\varphi}{\partial y_1}(y)+(x_2-y_2)\frac{\partial\varphi}{\partial y_2}(y)\right]exp\left(-\frac{\|x-y\|_2^2}{d^2}\right)$$

$$H(\varphi(y)+l)H\big(l-\varphi(y)\big)\,dy$$

where φ is the level set function, t the artificial time (iterations), α a constant velocity term of φ, SPF the signed pressure force function [44] that reflects the statistical information of the two regions of the image inside and outside the active contour. I is a given 2D image, x (x_1, x_2) and $y(y_1, y_2)$ are two neighbouring points on the active contour (the zero level set) as determined by the windowing function $\left(\exp\left(-\frac{\|x-y\|_2^2}{d^2}\right)\right)$, d is the width of the windowing function, μ a positive tuning parameter, H the regularized Heaviside function, and l the width of the narrow band around the zero level curve of φ (the active contour).

The resulting TPSBLS [45] segmentation algorithm in its all possible variants is similar to the one described above in

Fig. 4. 1. While φ will be updated using the resulting level set formulation (Eq. (4.3)) that minimizes the functional energy of the proposed model (Eq. (4.2)), TPSBLS model, is presented below It can be summarized in the following steps:

1. Set *n* initial contours Ω_i defined by an initial level set function $\varphi(x, t = 0)$ according to Eq. (4.1)),

2. Compute the SPF using Eq. (3.27).

3. Update $\varphi(x, t)$ using TPSBLS [45] formulation (Eq. (4.3)),

4. If (Local segmentation), set $\varphi(x, t) = 1$ for $\varphi(x, t) > 0$; and $\varphi(x, t) = -1$ otherwise.

   Else if (Global segmentation), jump to step 5,

5. Stop if $\varphi(x, t)$ has converged, otherwise return to step 2.

Hereafter, some results are presented using TPSBLS [45] for local segmentation; TPLBLS (Topology preserving local binary level set) [45] compared to those obtained with LBGFRLS and LBLS [45] with different levels of topology constraint, propagation speed α and the tuning parameter μ, applied on the same images used to test LBLS [45] performance (Fig. 4. 2).

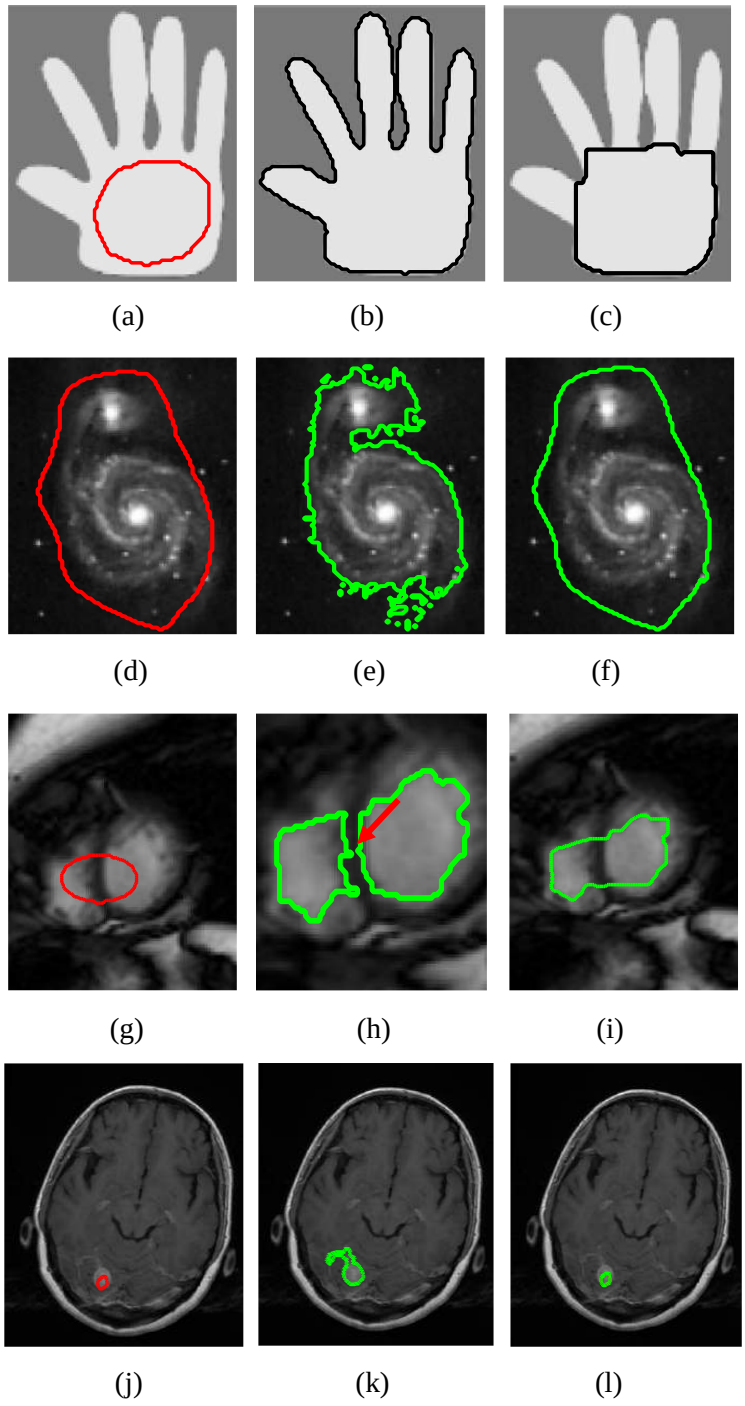

Fig. 4. 3. Segmentation results of TPLBLS [45]. Images with initial contour (a) - hand phantom, (d) - galaxy image, (g) - heart image from MICCAI 2012, and (j) - brain image from figshare dataset. (b), (e), (h) and (k) Segmentation results for α=20, $\mu = 0.5$ for (a) and (d), α=10, $\mu = 2.7$ for (g), α=20, $\mu = 0.5$ for (j). (c), (f), (i) and (l) Segmentation results for α=7, $\mu = 7$ for (a), α=20, $\mu = 5$ for (d), α=10, $\mu = 5$ for (g), α=20, $\mu = 35$ for (j). Initial contours are in red. Obtained contours in black and green.

For TPSBLS [45], α is set the same way as for the SBLS model [45], μ depends on α. We intentionally used the same images used before to test the SBLS model [45] (see Fig. 4. 2) and to demonstrate the enhancements brought by the proposed TPLBLS model [45]. In Fig. 4. 3, we kept the same value of α as in Fig. 4. 2 with smaller values of μ. More precisely, if μ is too small regarding α (e.g. Fig. 4. 2 (a) where α = 20 and μ = 0.5), TPLBLS model [45] successfully segmented the hand shape (Fig. 4. 3 (b) like the SBLS model (Fig. 4. 2 (c)). While for the two other images (Fig. 4. 3 (d) α = 20 and μ = 0.5 and Fig. 4. 3 (g): α=10 and μ = 2.7), the model shows significant deformations and important changes during the process of segmentation as can be clearly seen in Fig. 4. 3 (e) and (h). Results show more than one final contour, which is justified by the failure of the model to preserve the topology of its active contour. However, if the value of μ is relatively high (Fig. 4. 3 (a): α=7, μ=7, (d): α=20, μ=5, (g): α=10, μ=5 and α=20, μ=35 (j)), the influence of the topology constraints becomes dominant, which forces the model to preserve its topology and to remain close if not identical to the initial contour (Fig. 4. 3 (c), (f), (i) and (l)). In this case, segmentation results are not appropriate either. Finally, in Fig. 4. 4 setting μ to be smaller than α produces good segmentation results. One final contour that is homeomorphic to the initial one (Fig. 4. 4 (d), (e) and (f)). So, practically keeping μ relatively smaller than α encourages more flexibility in the TPLBLS model [45] and produces good segmentation results.

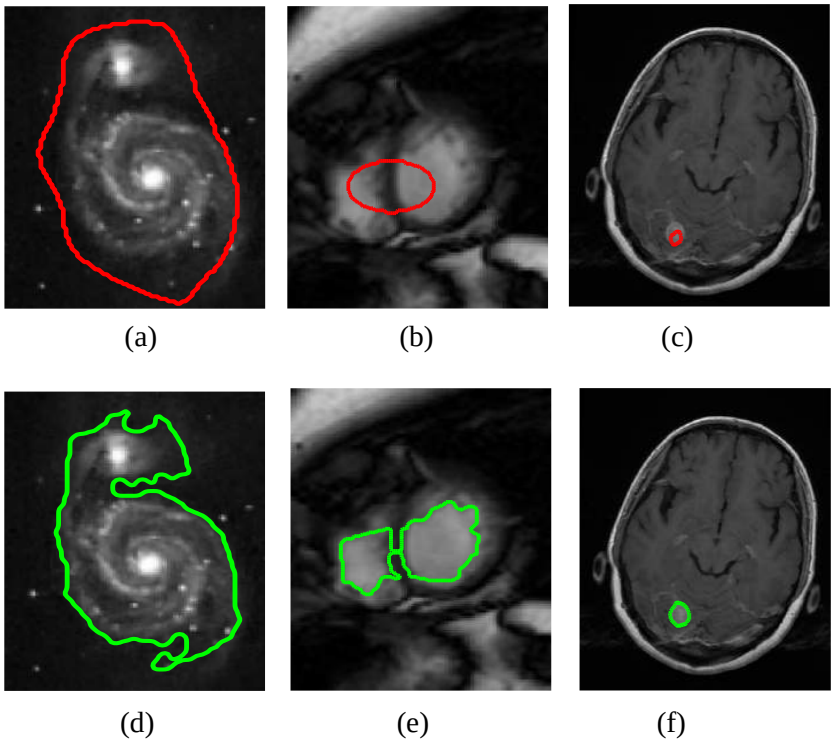

(a) (b) (c)

(d) (e) (f)

Fig. 4. 4. Segmentation results of TPLBLS [45]. Images with initial contour (a) - galaxy image, and (b) - heart image from MICCAI 2012. α=20, $\mu = 1$ for (a), α=10, $\mu = 3$ for (b). α=20, $\mu = 7$ for (c). Initial contour is in red. Obtained contour is in green.

4. 4 Conclusion

To summarize, this chapter provided two distinct approaches proposed during this thesis. The first segmentation approach is SBLS which enables to segment globally all existing objects in the image or locally one specific target but with a high possibility of failure caused by the automatic changes of the model's topology.

For that, we designed the second approach TPSBLS to involve a topology preserving term to constrain the automatic changing of its topology in a balanced way. Indeed coupling the model with a term based on the self-repelling force concept [41] to control the model's topology assures better results than those provided using SBLS or SBGFRLS [44].

Practically for both models LBLS and TPLBLS [45], both parameters α and μ should be set properly and relatively to the image itself for good results.

Chapter V

Results and discussion

5.1 Introduction

To validate the efficiency of the resulting algorithm using SBLS instead of SBGFRLS [44] and the efficiency of the proposed TPSBLS model [45], we used several real MRI slices of the heart from the RVSC dataset of MICCAI 2012 [47] and the Cardiac MRI of the York dataset 2006 [48] to segment the endocardium of one ventricle of the heart, MICCAI 2017 [49] database for bi-ventricular segmentation next to the figshare dataset [50] for brain tumor extraction. In all of the experiments presented in this section, the proposed models were applied on the original MRI slices with no training phase or preprocessing step.

5.2 Datasets

We used in our work four different datasets of real MRI. As described in chapter II, real MRI slices can contain different kinds of noises. Undoubtedly, the presence of noises can strongly and negatively affect the results of any processing. Therefore a pretreatment phase is indispensable for image denoising before any processing or analysis. Contrary to most of the

existing works, our approach doesn't require a pretreatment step. The different datasets used in this work are described below:

5.2.1 Cardiac MRI datasets

Several short axis cardiac MRI images of size 216×256 pixels from the RVSC dataset of MICCAI 2012 [47] were used to segment the right ventricle endocardium of a subject's heart. The data were acquired from June 2008 to August 2008 at Rouen University Hospital (France). Only the slices in the training set file of this dataset were accompanied by their corresponding ground truth (GT) of the right ventricle segmented manually (see Fig. 5.1(a)). We also used the Cardiac MRI dataset of the York dataset 2006 [48] which contains short axis cardiac MRI sequences of size 256x256 pixels with a pixel-spacing of 0.93–1.64 mm. This database was provided by the Department of Diagnostic Imaging of the Children's Hospital in Toronto for the purpose of testing the model's reliability to segment the endocardium of the heart left ventricle. The contours of the left ventricle were manually segmented by a trained operator to provide the corresponding GT as illustrated in the figure below (Fig. 5.1(b)). The third cardiac dataset is MICCAI 2017 [49] was launched during the Automatic Cardiac Diagnosis Challenge (ACDC) workshop held in conjunction with the 20th International Conference on Medical Image Computing and Computer Assisted Intervention (MICCAI), on September 10th, 2017 in Quebec City, Canada. It was created from real clinical exams acquired at the university hospital of Dijon over a 6 years period. It is composed of 150 patients (4 pathological plus 1 healthy subject groups). The spatial resolution goes from 1.37 to 1.68 mm^2/pixel and 28 to 40 images cover completely or partially the cardiac cycle. It includes manual expert segmentation of the right and left ventricles. The figure Fig. 5.1(c) shows an example of the dataset along with its corresponding manual segmentation.

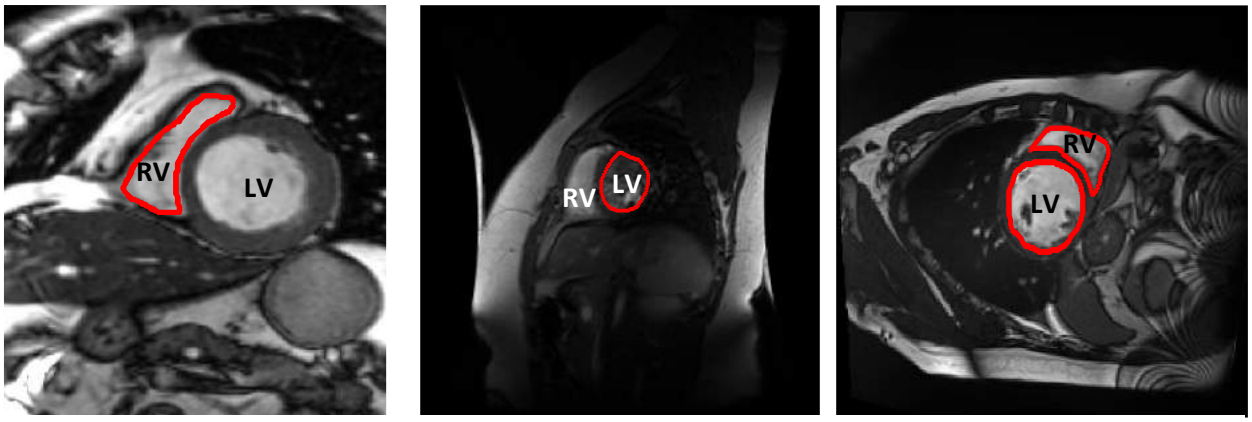

(a) (b) (c)

Fig. 5. 1. Slices from cardiac MRI datasets. (a) from MICCAI 2012 [47] dataset . (b) SUBJECT 25, slice 6-16 from York dataset 2006 [48]. (c) from MICCAI 2017 [49]. Ground truth (Manual segmentation of ventricle endocardium) is in red.

5. 2. 2 Brain MRI dataset

As for meningioma brain tumor segmentation experiments we used T1-weighted contrast-enhanced images from brain MRI figshare dataset [50] of 233 different patients. The brain T1-weighted dataset was acquired from Nanfang Hospital, Guangzhou, China, and General Hospital, Tianjing Medical University, China, from 2005 to 2010. The images have an inplane resolution of 512×512 with pixel size 0.49×0.49 mm^2. The slice thickness is 6 mm and the slice gap is 1 mm. The tumor border was manually delineated by three experienced radiologists (Fig. 5. 2). This dataset was used for validation of segmentation and classification approaches by several authors such as Rehman et al. [105] and Gupta et al.[106].

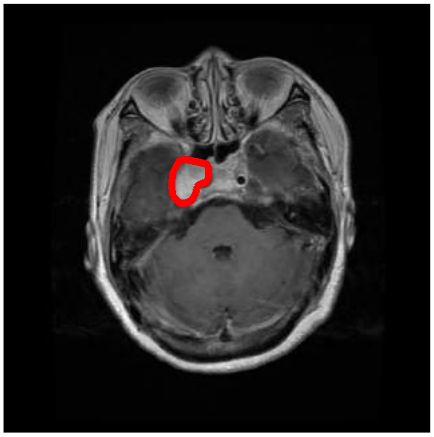

Fig. 5. 2. Patient 184 from brain MRI figshare dataset [50]. Ground truth (Manual segmentation of meningioma tumor) is in red.

5.3. Quantitative metrics for evaluation

The segmentation results of SBLS and TPSBLS were compared to their GT considering the original image for the four datasets described above; the RVSC dataset of MICCAI 2012 [47], the Cardiac MRI dataset of the York dataset 2006 [48], MICCAI 2017 [49] database of the Automatic Cardiac Diagnosis Challenge (ACDC) workshop and the brain MRI figshare dataset [50] using different metrics: Dice Coefficient (DC) [24], [41], Root Mean Square Error (RMSE) [22] and the Modified Hausdorff Distance (MHD) [107]–[109]. We also considered part of the same slices (66x71) round the Region Of Interest (ROI) of MICCAI 2012 datasets [47]. In what follows, we describe each one of the cited evaluation metrics:

DC is a common similarity metric defined by the following equation:

$$\mathrm{DC}(\mathrm{V_a}, \mathrm{V_m}) = \frac{2\mathrm{V_{am}}}{\mathrm{V_a} + \mathrm{V_m}} \tag{5.1}$$

where V_a, V_m and V_{am} are the manual segmentation of the ROI, segmentation using either SBLS or TPSBLS, and the intersection between them, respectively. DC is always within [0 1]

or [0% 100%]; 0 means no intersection between GT and the obtained results, while 1 (100%) means a perfect match.

RMSE evaluates the distance between segmented surfaces, defined as the surrounded area by the final contour resultant from the segmentation procedure, and the corresponding GT. The lower the RMSE, the better the conformity of the results to GT.

The RMSE over N points is given by:

$$\mathrm{RMSE} = \sqrt{\frac{1}{\mathrm{N}} \sum_{\mathrm{i}=1}^{\mathrm{N}} (\mathrm{x_i} - \grave{\mathrm{x}}_\mathrm{i})^2 + (\mathrm{y_i} - \grave{\mathrm{y}}_\mathrm{i})^2} \tag{5.2}$$

where N is the total number of points of the segmented surface, $(\grave{\mathrm{x}}_\mathrm{i}, \grave{\mathrm{y}}_\mathrm{i})$ a point on the segmented surface, and $(\mathrm{x_i}, \mathrm{y_i})$ the corresponding point on the manually traced surface.

The Hausdorff Distance (HD) [108] measures the closeness between two sets (S and T) rather than exact superposition; it is more tolerant towards disturbance in the locations of points. The HD is defined as:

$$\begin{cases} \mathrm{HD(S,T)} = \max\big(\mathrm{h(S,T)}, \mathrm{h(T,S)}\big) \\ \mathrm{h(S,T)} = \max_{\mathrm{n}\epsilon\mathrm{S}} \min_{\mathrm{m}\epsilon\mathrm{T}} \|\mathrm{n} - \mathrm{m}\| \end{cases} \tag{5.3}$$

where S and T are two different sets of points, and $\|n - m\|$ is the Euclidean distance between the elements of the two sets S and T. The contour pixels n and m run over S and T of indexes i and j. Since the HD is rather sensitive to noise, we opted to use a more robust version of this metric, namely MHD [107]–[109], defined as follows:

$$\begin{cases} \mathrm{MHD(S,T)} = \dfrac{1}{\mathrm{n}} \displaystyle\sum_{n\epsilon\mathrm{S}} \min_{\mathrm{m}\epsilon\mathrm{T}} \|\mathrm{n} - \mathrm{m}\| \\ \mathrm{MHD(T,S)} = \dfrac{1}{\mathrm{m}} \displaystyle\sum_{\mathrm{m}\epsilon\mathrm{T}} \min_{\mathrm{n}\epsilon\mathrm{s}} \|\mathrm{n} - \mathrm{m}\| \end{cases} \tag{5.4}$$

By taking the average of the single point distances, it decreases the impact of outliers which makes it more suitable for the evaluation of pattern recognition performances [107]–[109].

5.4. Experimental results

In this section we present two main applications of our proposed models; first, single object segmentation then two objects simultaneous segmentation. We show the strengths and the limits of the SBLS model next to the efficiency of the TPSBLS model as a solution to enhance the SBLS results when it fails. Both models are tested and evaluated for segmentation purposes vs. the manual segmentation outcomes and compared to the original SBGFRL and to other existing models in what follows:

5.4.1 Single object segmentation: Application to heart ventricle and brain tumor segmentation

In this section, we're interested more in local segmentation. Therefore we focused on some applications to experiment the ability of our proposed methods to segment a single target; one heart ventricle or a brain tumor. But we also presented briefly the behavior of their global variants during the segmentation process.

Considering the SBLS model [45] for segmentation, we present below examples of single ventricle segmentation in real heart images (from both MICCAI 2012 [47], and york dataset 2006 [48]) presented in Fig. 5. 3 and tumor extraction in real brain slices (from the brain MRI figshare dataset [50]) shown in Fig. 5. 4. Those figures show the SBLS [45] behavior of both kinds of its implementation; global implementation (GBLS [45]) which extracts all the

contours in the image and local implementation (LBLS [45]) capable of segmenting only the nearest objects to the initial contours.

Indeed for both GBGFRLS [44] and GBLS [45], the segmentation results of the left ventricle includes other surrounding contours in addition to that of the target in Fig. 5. 3(b), (c), (g), (h), (l) and (m) respectively, the right ventricle in Fig. 5. 3(q), (r), (v) and (w) and the brain tumor in Fig. 5. 4(b) and (c).

In Fig. 5. 3, the LBGFRLS approach failed to segment correctly the target alone, i.e. the left ventricle endocardium (Fig. 5. 3(d), (i) and (n)), the right ventricle endocardium (Fig. 5. 3(s) and (x)) and the tumor contour in Fig. 5. 4(d) instead, other undesired contours were segmented. This is due to the Gaussian filtering step originally set in the SBGFRLS model to regularize the level set function at each phase of the process. Applying the Gaussian smoothing repeatedly causes losing details of information imported by the model that are necessary for the next steps of the process. Indeed, skipping the Gaussian filtering step in the SBLS [45] brought to the model strength compared to the original SBGFRLS such as:

- Improving some of SBGFRLS segmentation results; SBLS model [45] correctly segmented the heart ventricle (see Fig. 5. 3(e), (j), (o) and (t)), as well the brain tumor (see Fig. 5. 4(e)).

- Eliminating one step of the algorithm reduces the computational cost which becomes important in case of processing high resolution images such as in our case.

For local segmentation of a single target (Heart ventricle in Fig. 5. 3 and brain tumor in Fig. 5. 4), LBLS [45] segments the closest object to the initial contour; the segmentation proceeds locally and only objects near to the initial contour will be considered for segmentation.

For example, in Fig. 5. 3 when the initial contour is intersecting (Fig. 5. 3(a)), inside (Fig. 5. 3(f)) or surrounding (Fig. 5. 3(k)) the target, i. e. the left ventricle, the LBLS model [45]

succeeded in extracting the target alone (Fig. 5. 3(e), (j) and (o), respectively). The same thing goes for brain tumor segmentation in Fig. 5. 4(e). However in Fig. 5. 3(u), the process extracted a different object instead of the target, i.e. the right ventricle (see Fig. 5. 3(y)).

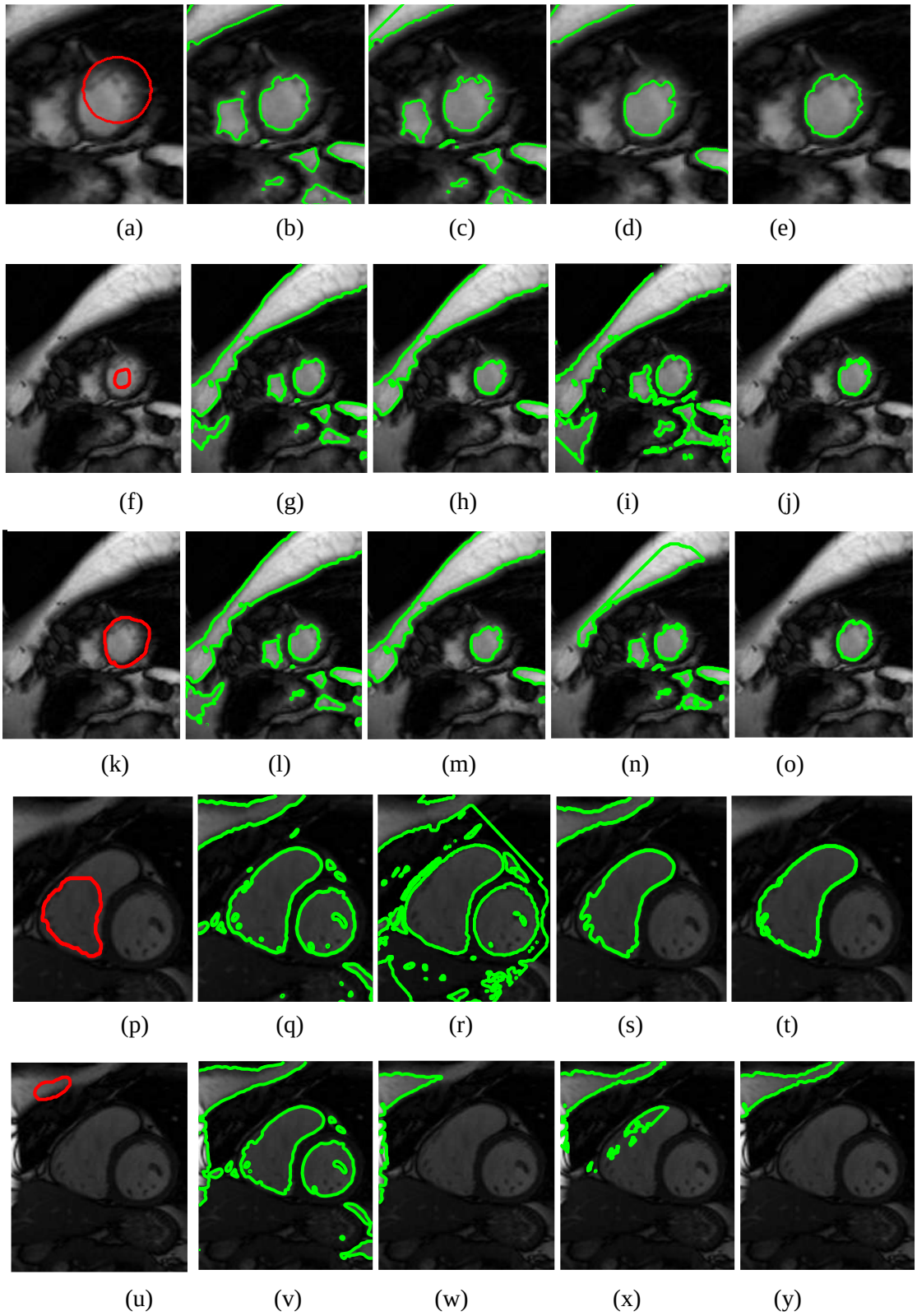

Fig. 5. 3. Segmentation results of GBGFRLS, GBLS [45], LBGFRLS and LBLS [45]. Images with initial contour (a), (f) and (k) heart image from York dataset 2006, (p) and (u) -heart image from MICCAI 2012. GBGFRLS segmentation results (b), (g), (l), (q) and (v). GBLS [45] segmentation results (c), (h), (m), (r) and (w). LBGFRLS segmentation results (d), (i), (n), (s) and (x). LBLS segmentation results (e), (j), (o), (t) and (y). Initial contours are in red. Obtained contours are in green.

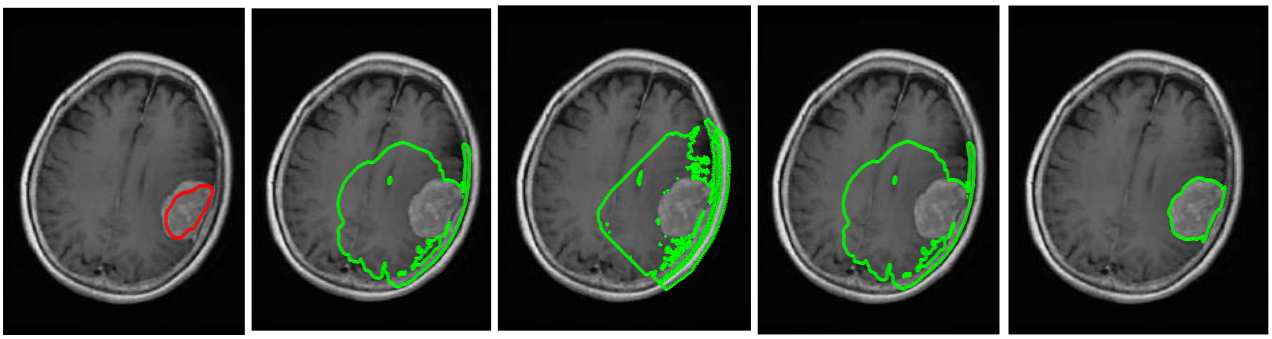

(a) (b) (c) (d) (e)

Fig. 5. 4. Segmentation results of GBGFRLS, GBLS [45], LBGFRLS and LBLS [45]. Images with initial contour (a) –Brain image from brain MRI figshare dataset. GBGFRLS segmentation results (b). GBLS segmentation results (c). LBGFRLS segmentation results (d). LBLS [45] segmentation results (e). Initial contours are in red. Obtained contours are in green.

For several cardiac MRI slices, even LBLS [45] failed to segment its target. This was the case of the left ventricle of the heart (Fig. 5. 7 (c) and (g)), the right ventricle (Fig. 5. 7 (k) and (o)) and the brain tumor (Fig. 5. 10(d), (i) and (n)), for example, where the topology of the active contour changed automatically. Indeed, the segmentation process ended up with a contour of a different topology compared to the initial one, in addition to undesirable contours. In this case our proposed TPLBLS [45] is highly recommended for both heart ventricles (Fig. 5. 7(d), (h), (l) and (p)) and brain tumor segmentations (Fig. 5. 7(e), (j) and (o)).

Globally and for the evaluation of the local variants of both the LBLS and TPLBLS models [45], we considered only the slices provided with their corresponding manual segmentations: GT.

We randomly used 73 slices from RVSC MICCAI 2012 [47] for the segmentation of the right ventricle endocardium, 176 images from the York dataset 2006 [48] for the segmentation of the left ventricle endocardium and 158 slices from the brain MRI figshare dataset [50] in order to evaluate and compare the efficiency of the local segmentation

achieved by our proposed LBLS and TPLBLS approaches [45]. The proposed methods were also compared to existing models such as GAC [28], CV [31], TGDM [27] and SBGFRLS [44] for heart ventricle and brain tumor segmentations in the same slices using the same conditions of initialization. For all experiments the parameters *l* and *d* in Eq. (7) were set to 1.

The following figures (Fig.5. 5 and Fig.5. 6) show the performance of each one of the techniques mentioned earlier. It's described using Dice values corresponding to the segmentation outcome of each one of the slices taken from the York dataset 2006 [48] and RVSC MICCAI 2012 [47] respectively.

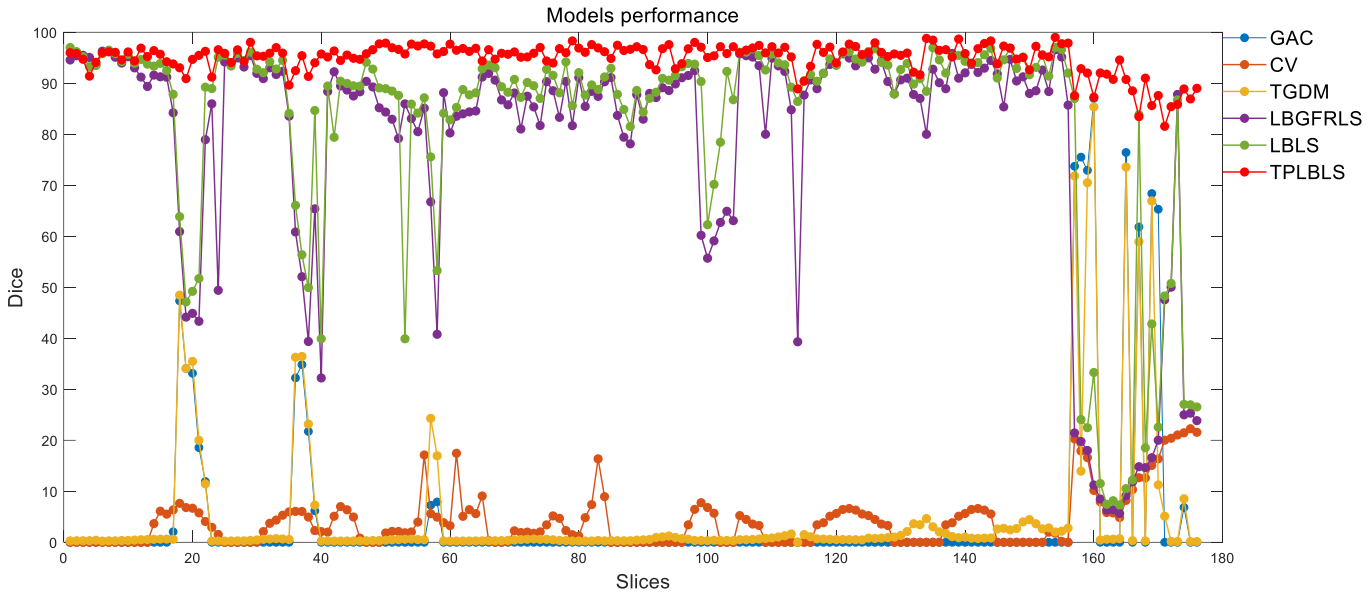

(a)

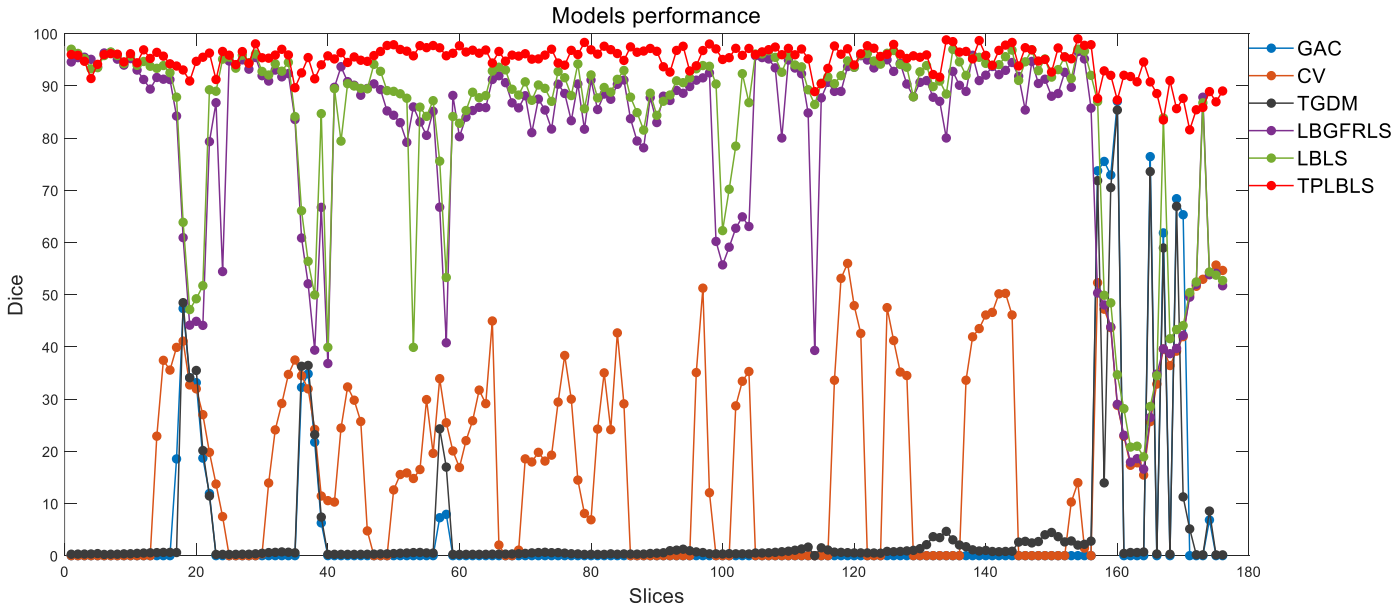

(b)

Fig. 5. 5. Dice variation of left ventricle segmentation results using GAC, CV, TGDM, LBGFRLS, LBLS and TPLBLS models [45]. (a). Original slices (256x256 pixels) from York dataset 2006, (b). Parts of slices (66x71 pixels) from York dataset 2006.

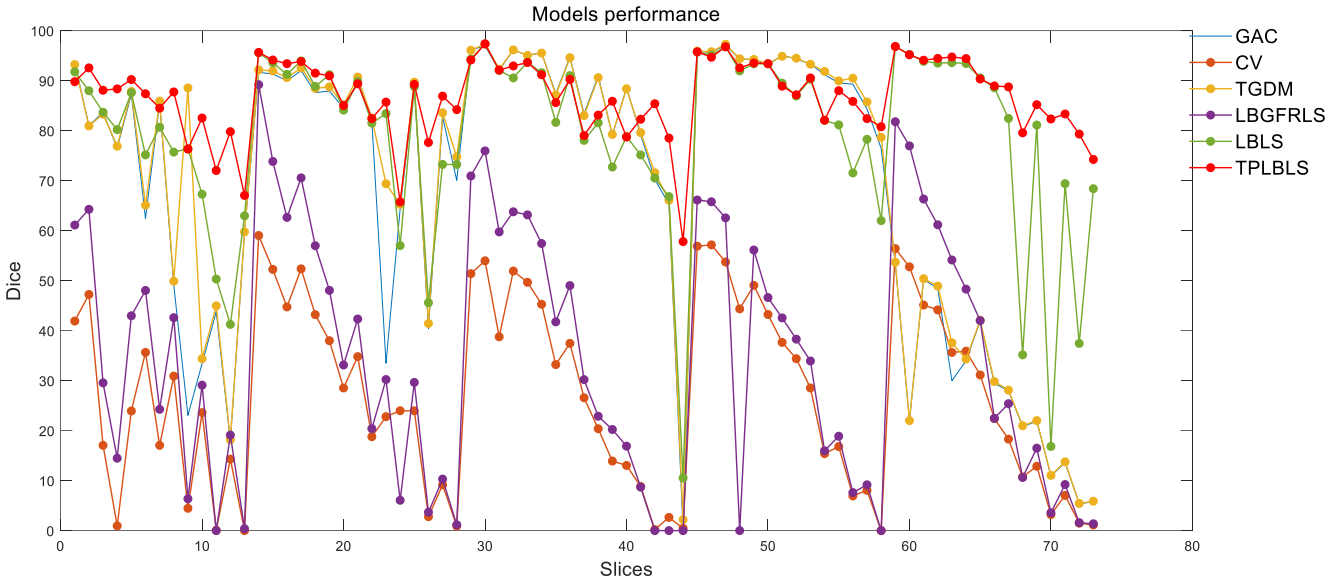

Fig. 5. 6. Dice variation of left ventricle segmentation results in original slices (256x216 pixels) from MICCAI 2012 using GAC, CV, TGDM, LBGFRLS, LBLS and TPLBLS models [45].

Furthermore, Table 1 reports the overall mean and standard deviation of the quantitative evaluation of the proposed methods LBLS and TPLBLS [45] as well as the existing models cited above using DC, RMSE and MHD. The first table includes both segmentation results of single target; left ventricle endocardium for the York dataset 2006 [48] and right ventricle endocardium for RVSC MICCAI 2012 [47]. As the slices from the York dataset 2006 [48] include considerable unnecessary background, we also considered parts of each image (66x71) that contain the segmented target and less of the background.

Table 1: Mean and Standard Deviation of quantitative evaluation of LBLS and TPLBLS methods [45] using DC, RMSE and MHD metrics of single ventricle segmentation of cardiac MRI.

		Left ventricle segmentation		**Right ventricle segmentation**
Metric	**Approach**	**Image(256x256)**	**Image (66x71)**	**Image (216×256)**
DC	**GAC**	4.802±16.298	4.897±16.331	68.24±29.539
	CV	4.143±5.253	18.149±18.229	27.268±18.621
	TGDM	5.024±14.420	5.026±14.421	70.237±28.617
	SBGFRLS	77.978.131±24.481	80.236±19.539	34.604±25.572
	LBLS	82.300±22.290	83.873±18.193	79.496±18.220
	TPLBLS	94.925±3.023	94.925±3.023	86.773 ±7.687
RMSE	**GAC**	0.160±0.059	0.300±0.100	0.176±0.128
	CV	0.318±0.115	0.428±0.177	0.448±0.0850
	TGDM	0.073±0.027	0.301±0.100	0.168±0.124
	SBGFRLS	0.073±0.099	0.212±0.071	0.332±0.072
	LBLS	0.061±0.081	0.187±0.17	0.214±0.236
	TPLBLS	0.023±0.009	0.084±0.032	0.0927±0.0236
MHD	**GAC**	1.235±0. 708	1.550±0. 739	1.267±1.305
	CV	3.578±1.976	2.275±1.567	5.984±0.922
	TGDM	0.392±0.190	1.516±0. 730	1.169±1.232
	SBGFRLS	0.534±1.183	1.044±1.577	3. 752±1.149
	LBLS	0.405±0.929	0.920±1.448	0.469±0.319
	TPLBLS	0.0725±0.053	0.281±0.206	0.472±0.195

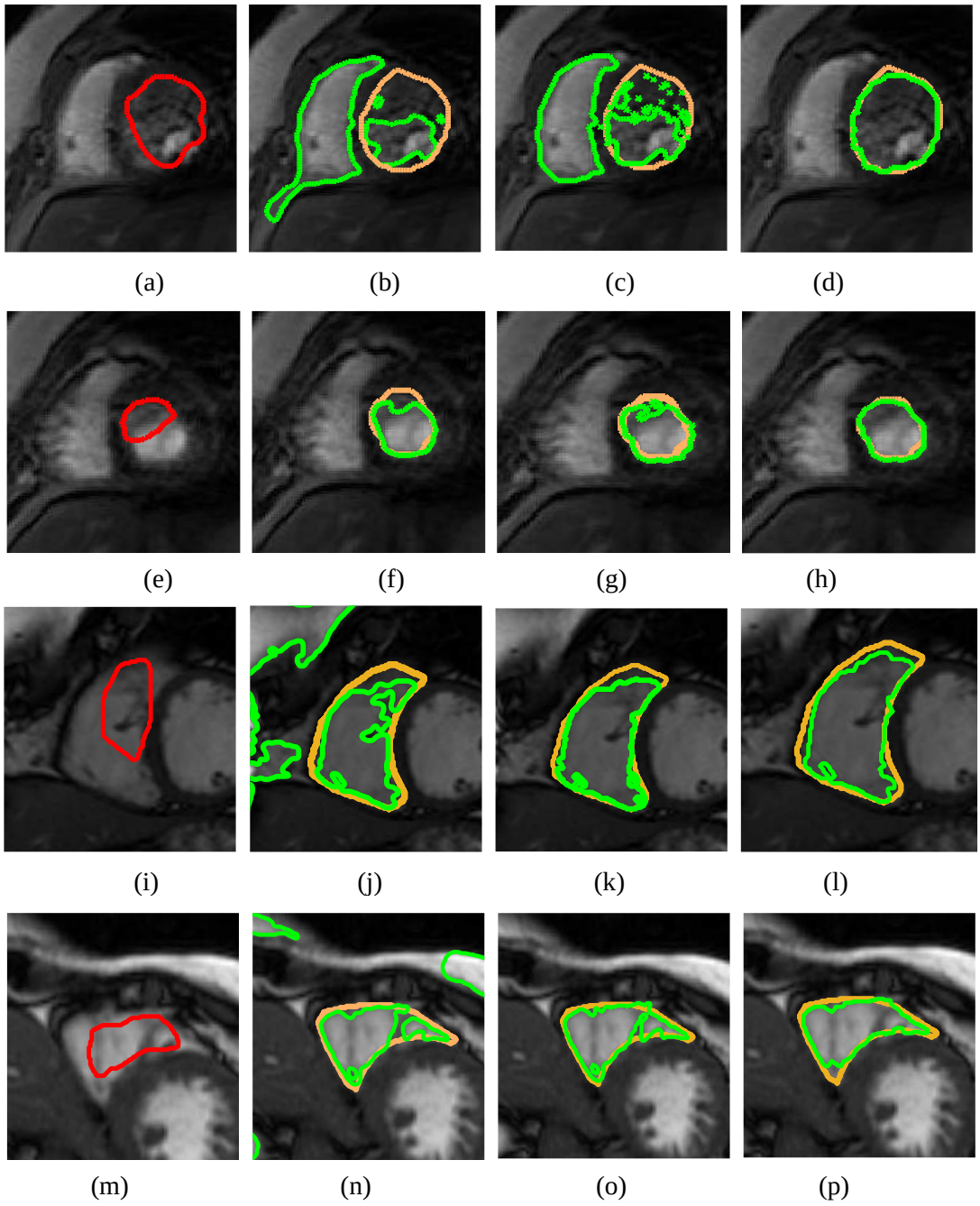

Fig. 5. 7. Segmentation results of LBGFRLS, LBLS and TPLBLS [45]. Images with initial contour (a) and (e) -heart image from the York dataset. (i) and (m) - heart image from MICCAI 2012. LBGFRLS segmentation results (b), (f), (j) and (n). LBLS segmentation results (c), (g), (k) and (o). TPLBLS segmentation results (d), (h), (l) and (p). (b) DC=33.218, (c) DC=39.9, (d) μ=7, DC=95.7, (f) DC=84.21, (g) DC=87.8, (h) μ=4, DC=93.8, (j) DC=89.49, (k) DC=88.89, (l) μ=4, DC=42.55, (n) DC=48.5, (o) DC=89.5, (p) μ=7, DC=88.9, The GT is represented in orange. Initial contours are in red. Obtained contours are in green.

In the figure below we present an example of a ventricular volume based on some final 2D segmentations of left ventricle in successive slices using LBGFRLS [44], LBLS and TPLBLS [45].

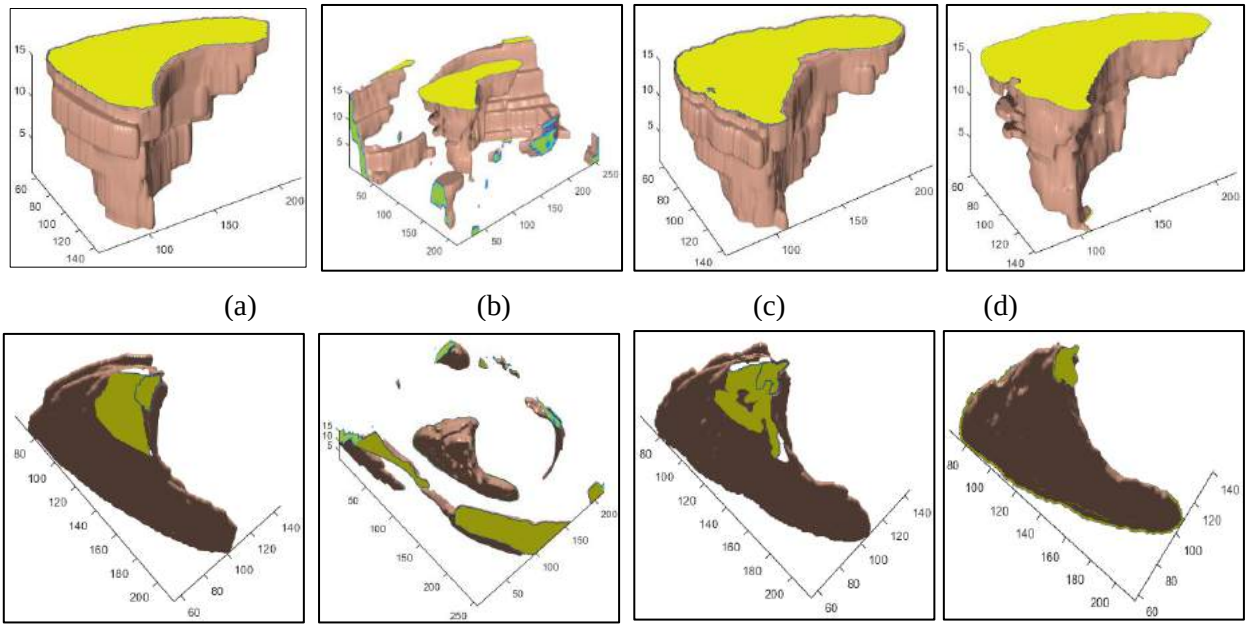

(a) (b) (c) (d)

(e) (f) (g) (h)

Fig. 5. 8. Volume representation of Left ventricle Segmentation results of LBGFRLS, LBLS and TPLBLS [45]- heart images of patient P02 from MICCAI 2012 dataset. (i) and (m). Manual segmentations (a) and (e). LBGFRLS segmentation results (b) and (f). LBLS segmentation results (c) and (g). TPLBLS segmentation results (d) and (h).

The total processing time (t) may vary from a slice to another even from the same dataset. This is due to many factors such as size of the image, size of the initial contour, size of the target, parameters α, μ, etc. However, the total processing time per slice is reasonably small, around a second if not less. The processing time in seconds of SBGFRLS [44], SBLS and TPSBLS is reported in Table 2.

Table 2: Total processing time in seconds for slices of Fig. 5. 7.

SBGFRLS [44]		SBLS [45]		TPSBLS [45]	
(b)	0.764	**(c)**	0.692	**(d)**	0.263
(f)	0.369	**(g)**	0.350	**(h)**	0.348
(j)	0.719	**(k)**	0.524	**(l)**	0.555
(n)	1.208	**(o)**	0.353	**(p)**	0.279

The following figure (Fig**. 5. 9**) show the performance of our proposed LBLS and TPLBLS approaches [45] and some existing models: GAC [28], CV [31], TGDM [27] and SBGFRLS [44]. It's described using Dice values corresponding to the brain tumor segmentation results.

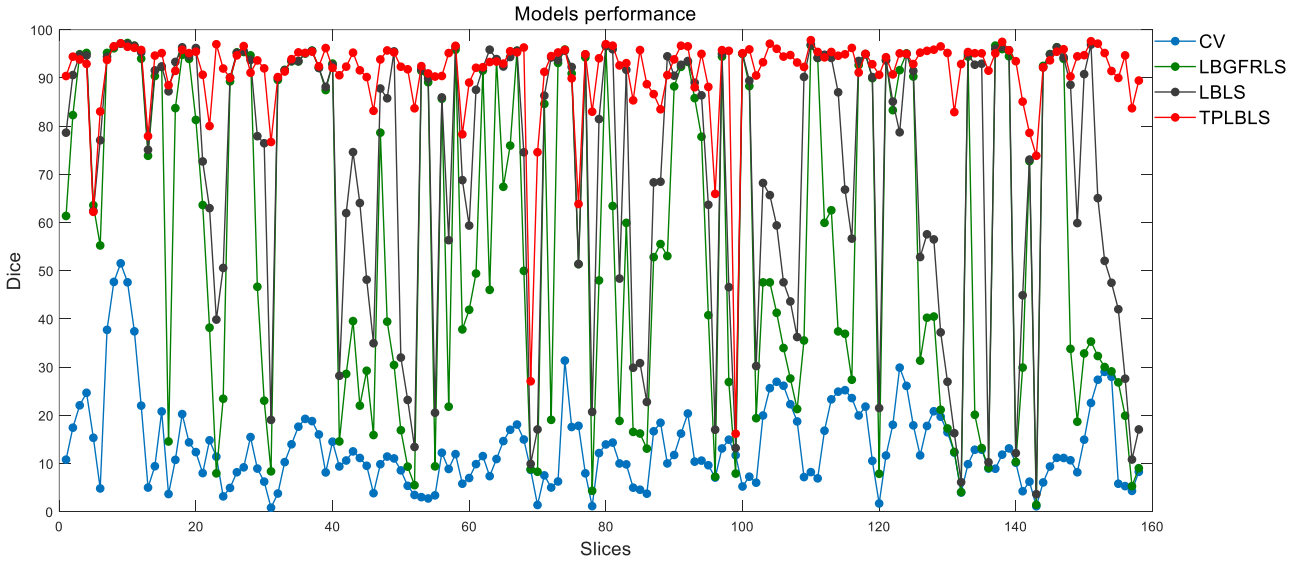

Fig. 5. 9. Dice variation of brain tumor segmentation results in original slices (256x216 pixels) from brain MRI figshare dataset using CV, LBGFRLS, LBLS and TPLBLS models.

The table below illustrates the evaluation metrics of the meningioma tumor segmentation results in slices from the brain MRI figshare dataset [50].

Table 3: Mean and Standard Deviation of quantitative evaluation of LBLS and TPLBLS methods [45] using DC, RMSE and MHD metrics of meningioma brain tumor segmentation.

Approach \ Metric	DC	RMSE	MHD
CV	13.4250±8.8636	0.4863±0.1002	8.3144±1.8008
SBGFRLS	57.4164±33.6748	0.1922±0.1584	2.4492±2.5341
LBLS	71.6977±28.1775	0.1179±0.1061	1.2270±1.5351
TPLBLS	90.9822±9.9616	0.0493±0.0315	0.3103±0.4776

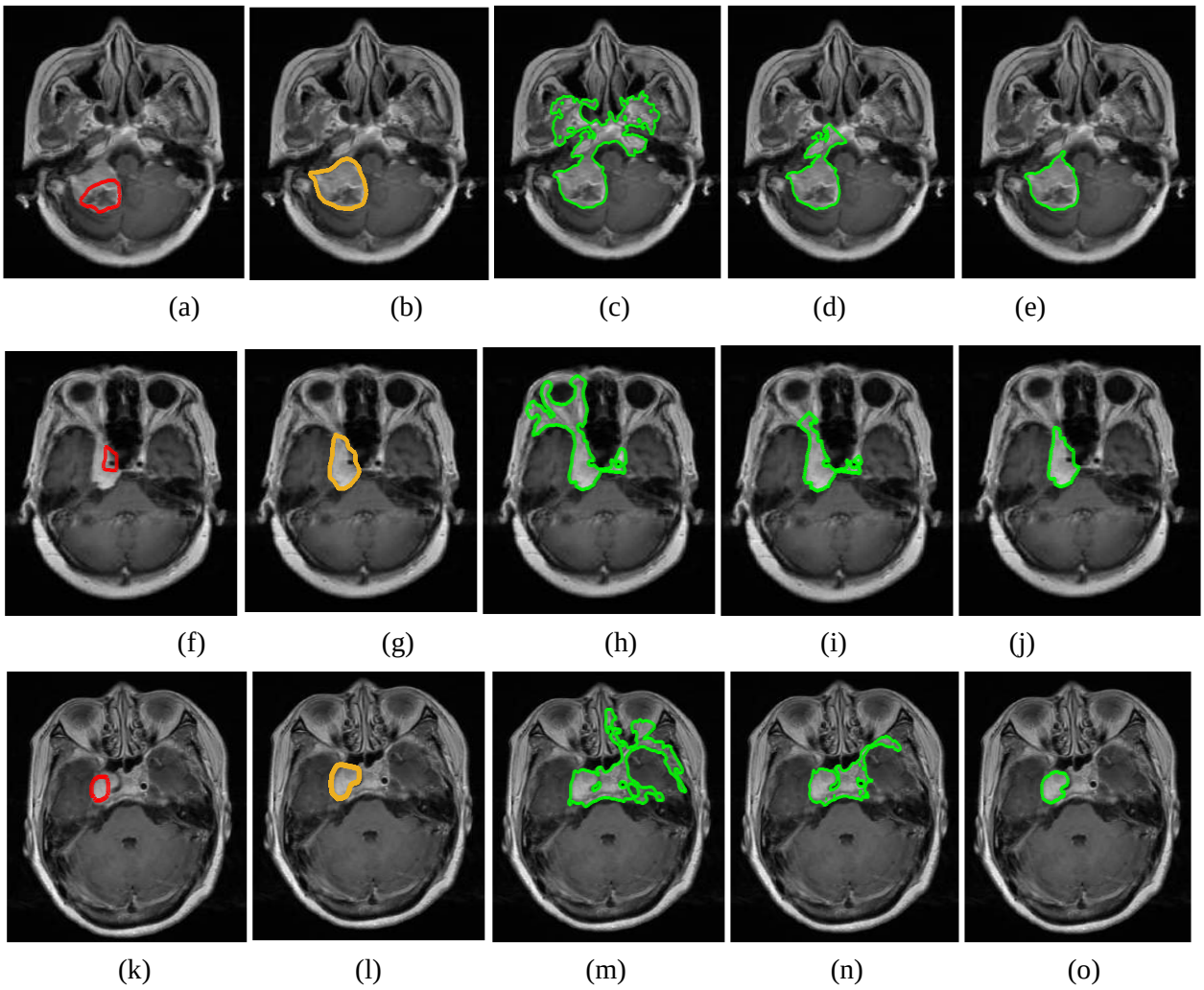

Fig. 5. 10. Segmentation results of LBGFRLS, LBLS and TPLBLS. Images with initial contour (a), (f) and (k) -brain MRI image from the figshare dataset. GT (b), (g) and (l). LBGFRLS segmentation results (c), (h) and (m). LBLS segmentation results (d), (i) and (n). TPLBLS segmentation results (e), (j) and (o). (c) DC=47.9847, (d) DC=81.4617, (e) μ=8, DC=94.0771, (h) DC=46.6703, (i) DC=77.9165, (j) μ=12, DC=93.6359, (m) DC=29.903, (n) DC=44.902, (o) μ=12, DC=85.078. The GT is represented in orange. Initial contours are in red. Obtained contours are in green.

As can be seen on table 1 and 3, the TPLBLS model [45] gives better results than LBLS [45]. Note also that, in general, the LBLS model without a topology controlling term seems to be capable of providing good numbers as well. However, in addition to undesired contours, the results for the segmented objects are not satisfactory. They are not so close to the boundaries of the target segmented manually (For example Fig. 5. 7(g) and (o) and Fig. 5. 10(s)), even though the corresponding DC seems to be acceptable: 87.8, 89.5 and 59.88 respectively. Not to mention the presence of unexpected contours. This is due to the fact that

the initial contour was splitting during its evolution. Unlike LBLS [45], the improved TPLBLS model [45] preserves the topology of the evolving contour along with the segmentation process. Indeed, the final contour is homeomorphic to its corresponding one set initially (Fig. 5. 7(d), (h) and (p)), for example, with the corresponding DC: 95.7, 93.8 and 88.9, respectively, as well as in Fig. 5. 10(e), (j) and (o) with the corresponding DC: 94.0771, 93.6359 and 85.078, respectively). The worst segmentation results were provided by SBGFRLS (Fig. 5. 7(b), (j) and (n)) for heart ventricle segmentation while all of the MRI slices in Fig. 5. 10 SBGFRLS completely failed to segment the brain tumor.

Globally and according to table 1 and 3 above, our proposed methods (LBLS and TPLBLS) achieve better values of DC and lower values of RMSE and MHD than the GAC [28], CV [31], TGDM [27] and SBGFRLS [44] models. Table 1 shows also that both GAC [28] and TGDM [27] are more suitable for the MICCAI 2012 dataset than the York dataset 2006 [48], contrary to SBGFRLS [44]. This can be explained by the fact that the York dataset 2006 slices have thinner contours compared to the MICCAI 2012 slices and GAC [28] and TGDM [27] originally require a good quality of image contours while SBGFRLS is a region-based model. However, CV approach provides weak results for both datasets.

5.4.2 Two objects simultaneous segmentation: Application to bi-ventricular segmentation of cardiac MRI

Our proposed LBLS [45] is able to segment, simultaneously, a specific number of different targets by initiating the same number of contours; LBLS [45] successfully segmented, in a real heart slice from the York dataset 2006 [48], two segmented objects using two initial contours (Fig. 5. 11(c)) and three targets (Fig. 5. 11(f)) after initiating the process with three contours. In comparison, LBGFRLS gives four final contours (Fig. 5. 11(b) and (e)) instead of two and three contours, respectively.

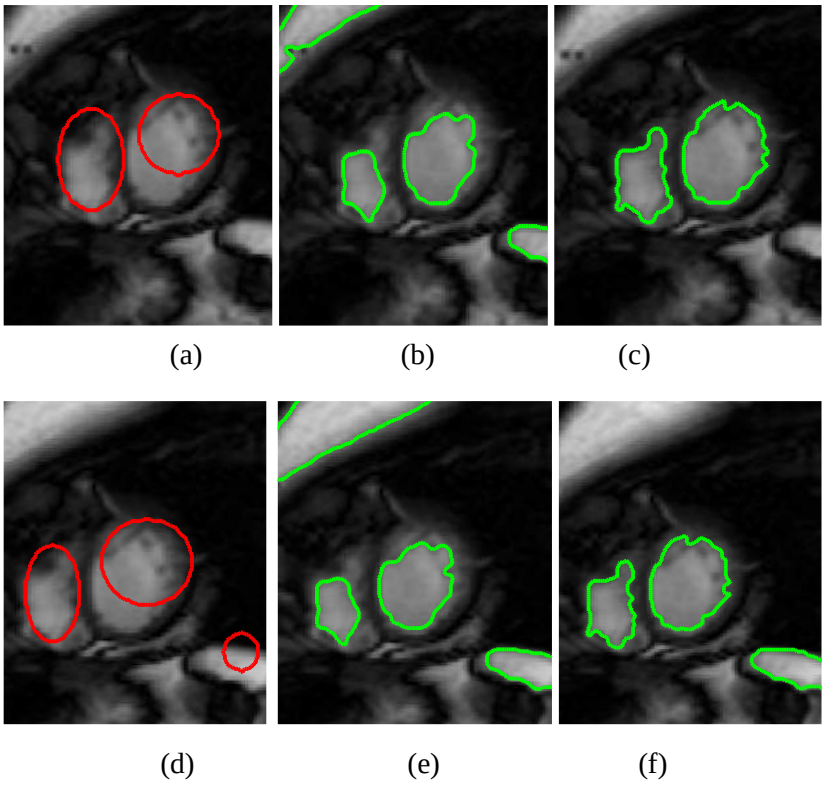

Fig. 5. 11. Segmentation results of LBGFRLS and LBLS. Images with initial contour (a) and (d) -heart image from the York dataset. LBGFRLS segmentation results (b) and (e). LBLS segmentation results (c) and (f). Initial contours are in red. Obtained contours are in green.

Our TPLBLS model [45] is also able to segment N specific objects simultaneously. To illustrate, it was applied to segment the two ventricles simultaneously (Fig. 5. 12 (d) and (h)) as in [24], where the authors presented an approach for simultaneous left and right ventricle segmentation using topology preserving level sets. We first used some slices from RVSC MICCAI 2012 [47] to test the performance of our TPLBLS [45] to segment left and right ventricles simultaneously starting with two separate initial contours. As can be seen in the following figure, the best segmentation results were provided by TPLBLS (Fig. 5. 12(d) and (h)) rather than by LBLS (Fig. 5. 12(c) and (g)) which in turn gave better results than SBGFRLS [44] (Fig. 5. 12(b) and (f)). The segmentation with TPLBLS seems to be the closest to the boundaries of the target and preserved the topology of the evolving contour.

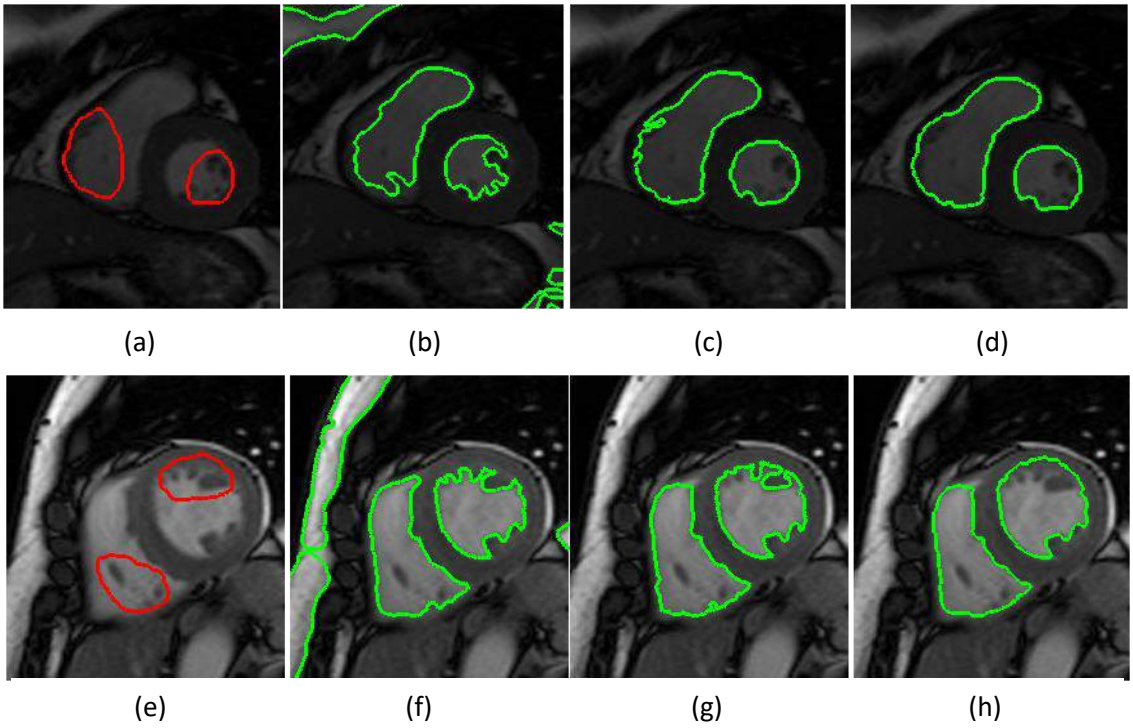

Fig. 5. 12. Simultaneous left and right ventricle segmentation results of LBGFRLS, LBLS, TPLBLS. Images with initial contour (a) and (e) - heart image from MICCAI 2012. LBGFRLS segmentation results (b, f), LBLS segmentation results (c, g). TPLBLS segmentation results (d, h). Initial contours are in red. Obtained contours are in green.

However, for quantitative validation we needed a cardiac dataset MRI that provides manual annotations of both ventricles. Therefore, we used the cardiac database MICCAI 2017 [49] for biventricular segmentation to prove in numbers the reliability and applicability of the proposed models. Since the database provides manual segmentation of both ventricles endocardium we could estimate the mean and the standard deviation of DC, RMSE and MHD metrics of the results and compare them to the existing techniques; CV[31] and SBGFRLS [44] (see table 4).

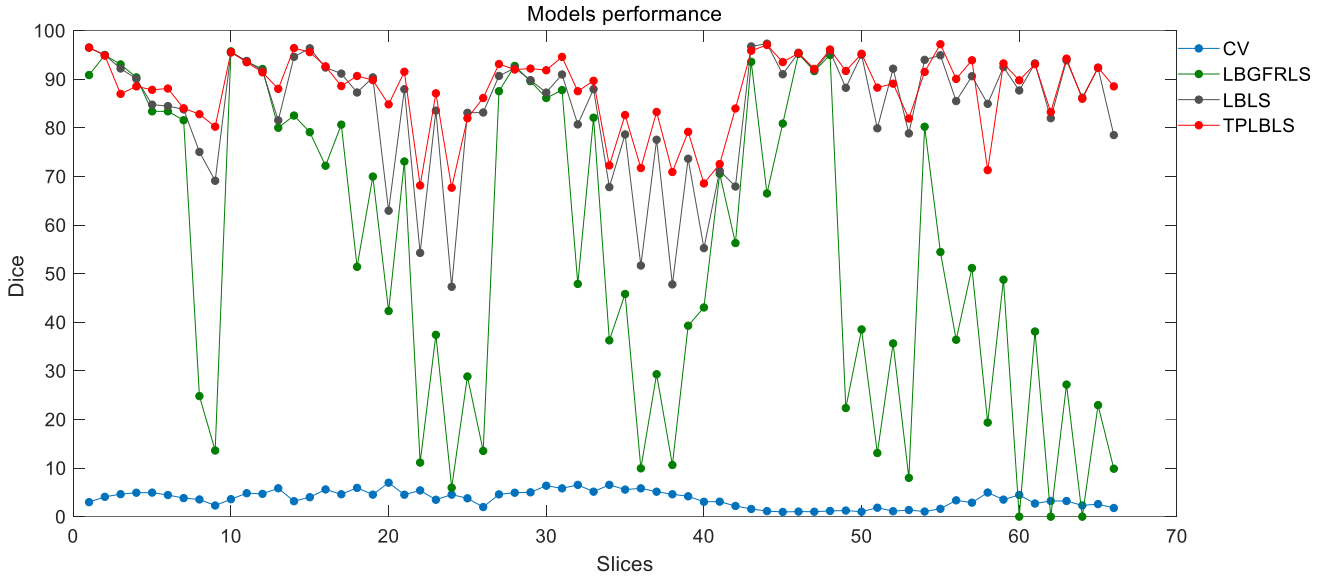

Fig. 5. 13. Dice variation of bi-ventricular segmentation results in slices from MICCAI 2017 dataset using CV, LBGFRLS, LBLS and TPLBLS models.

Table 4: Mean and Standard Deviation of quantitative evaluation of LBLS and TPLBLS methods [45] using DC, RMSE and MHD metrics of bi-ventricular segmentation for 66 slices from MICCAI 2017 [49] cardiac MRI.

Approach \ Metric	DC	RMSE	MHD
CV	3.6797 ± 1.6696	0.9144± 0.0252	13.0061± 0.6513
SBGFRLS	54.6860± 31.8672	2.1156± 0.8245	0.3030± 0.0635
LBLS	84.2088±12.4021	1.4691±0.6499	0.2491±0.0716
TPLBLS	87.6712±7.8512	1.4521±0.6595	0.2433±0.0730

Similarly to the segmentation results in section 5.4.1, TPLBLS and LBLS approaches were more useful for bi-ventricular segmentation based on their results which are clearly better than those achieved by LBGFRLS [44] and CV [31] methods (see Fig. 5. 10). As it's illustrated in table 4 the evaluation metrics values of LBLS results (DC: 84.21, RMSE: 1.47 and MHD:

0.25) seem to be close to those of TPLBLS results (DC: 87.67, RMSE: 1.45 and MHD: 0.24). Whereas, the performance provided by the latter approach is the closet to the manual segmentation giving at the end of the process final contours that are homeomorphic to the initiation thanks to its topology constraining term. For instance, in Fig. 5. 10 (q) LBLS result is of a good DC value (81.54) however it gives numerous contours while it's supposed to give only the biventricular contour that surrounds both ventricles. TPLBLS, for the same example, (Fig. 5. 10 (q)) successfully achieved biventricular segmentation with no extra contours with a DC of 88.03. Globally, when considering only the evaluation metrics, the worst results were obtained by means of CV [31] model (DC: 3.68, RMSE: 0.91 and MHD: 13), but when considering the number of resultant contours the best results are definitely those of TPLBLS thanks to its capability of preserving the topology of the deformable model.

Fig. 5. 14. Simultaneous left and right ventricle segmentation results of CV, LBGFRLS, LBLS and TPLBLS. Images with initial contour (a), (g), (m) and (s) - heart image from MICCAI 2017. GT (b), (h), (n) and (t). CV segmentation results (c), (i), (o) and (u). LBGFRLS segmentation results (d), (j), (p) and (v). LBLS segmentation results (e), (k), (q) and (w). TPLBLS segmentation results (f), (l), (r) and (x). (c) DC= 3.1760 , (d) DC= 82.5265 , (e) DC= 94.6113, (f) μ=12, DC= 96.3986 , (i) DC= 6.9859, (j)) DC= 42.3077, (k) DC= 62.9482, (l) μ= 12, DC= 84.8168, (o) DC= 5.8365, (p)) DC= 80.0149, (q) DC= 81.5413, (r) μ= 8, DC= 88.0250, (u) DC= 1.5775 , (v)) DC= 54.4517, (w) DC= 94.9314 , (x) μ=5, DC= 97.1878. Initial contours are in red. Obtained contours are in green.

5.5. Conclusion

In this chapter, we have presented the experimental results of our approaches for heart ventricle and brain tumor segmentation. We have applied the two proposed SBLS and TPSBLS models for local segmentation of a single target: cardiac structures (one ventricle; right or left), brain structure anomaly (meningioma tumor) and two targets simultaneously (right and left ventricles of cardiac MRI). Real MRI slices of different databases, providing their manual segmentations, were used to evaluate our approaches. The obtained evaluation metrics values of the experimental results on both cardiac and brain MRI datasets prove the efficiency of our proposed SBLS model and even more when using the proposed TPSBLS in the same conditions as with LBLS. Indeed, it's demonstrated that the TPSBLS, in its local mode, overcomes LBLS weakness (automatic topology changing of the active contour) which, consequently, leads to more accurate target extractions. In order to better assess our approach and to highlight its strengths and weaknesses we also have presented a comparative study with some existing models reported in the literature. Indeed both SBLS and TPSBLS approaches succeeded all of the other ones implemented in this chapter.

Conclusion and perspectives

Image segmentation has been considered as a vital step in medical image analysis to detect and identify several pathologies and/or organ abnormalities. This dissertation concerns segmentation of real medical images segmentation by means of two important geometric deformable models, suitable for real cardiac and cerebral MRI slices precisely.

In a theoretical part, we presented the MRI technique starting by its evolution in history, its acquisition techniques along with its advantages and limitations. Then, we introduced a literature review of some existing techniques for medical image segmentation in order to evaluate our approaches compared to existing methods. Therefore, we first provided a theoretical background of both types of the DMs: PDMs and GDMs which demonstrates that the GDMs have been extensively studied and widely used in medical image segmentation with interesting results [10], [11] due to several advantages over PDMs such as their intrinsic behavior, ease of implementation and ability to handle automatic topology changes. Thus, we focused on GDMs as a more suitable model for our work. Second, we were interested in some topology preserving concepts that can be exploited to constrain the GDM's flexibility, which, in our case of medical image segmentation, becomes a liability. Indeed, the integration of a topology control concept helps to guide the evolving model in a way that preserves its topology during the segmentation process.

In the rest of this thesis, we described, in detail, our two proposed deformable models for heart ventricles and meningioma brain tumor segmentation in MRI slices. We first presented the proposed SBLS model that is based on SBGFRLS [44]. It successfully provides either global or local segmentations with no requirement of a preprocessing phase. Unlike SBGFRLS [44], SBLS does not involve regularization of the level set function by means of a Gaussian filter. This speeds up the segmentation process as can be seen in table 2. Moreover, when applying SBGFRLS for local segmentation, the Gaussian filtering step may give additional contours beside the desired ones. Contrary to SBGFRLS [44], in its local variant, LBLS is able to segment not just a single contour but it can also control the number of objects to be segmented simultaneously among all the existing ones by using as many initial contours as needed.

Second, we presented the other model: TPSBLS. It was proposed to enhance the segmentation results achieved using the SBLS approach. TPSBLS is the result of a successful combination of the previous SBLS model with the self-repelling force concept which serves to constrain the topology of the active contour in a way that is neither dominant nor inefficient. TPSBLS model doesn't involve any preprocessing step. It is also a selective model such as SBLS; it is able to ensure a global (TPGBLS) or a local segmentation (TPLBLS).

In order to evaluate and compare the efficiency of the local segmentation achieved by means of both proposed models LBLS and TPLBLS, we tested each one of them on real MRI slices provided with theirs corresponding manual segmentations: GT from four different datasets; We randomly used 73 slices from RVSC MICCAI 2012 [47] for the segmentation of the right ventricle endocardium, 176 images from the York dataset 2006 [48] for the segmentation of the left ventricle endocardium, 158 slices from the brain MRI figshare dataset [50] for the brain tumor extraction and finally 66 cardiac MRI from MICCAI 2017 [49].

The segmentation results of LBLS were compared to the GT. Table 1 shows the mean values of different metrics used for evaluation and quantitative validation. For left ventricle segmentation, the DC similarity between LBLS segmentation and the GT is about 88%, the RMSE value is 0.036 while MHD is about 0.117. Using the same LBLS for right ventricle endocardium segmentation, the evaluation metrics are: DC around 80%, RMSE of 0.105 and MHD of 0.56. The results of meningioma segmentation are reported by Table 3 as follows: DC is about 71.7%, RMSE value is 0.1179 and MHD is 1.227. Table 4 presents the outcome of simultaneous segmentation of both cardiac ventricles; DC: 84.21%, RMSE 1.47 and MHD 0.25. These results are quite satisfying. However, on analyzing different slices, local segmentations of ROIs using LBLS show that, in many slices, the initial contour underwent considerable automatic topology changes. This negatively affects the evolution of the active contour and consequently leads to undesired final contours. Thus we've opted for a better orientation of the active contour in the purpose of preventing undesired behavior of our model and obtaining more correct and accurate segmentation results at the end of the process. TPLBLS is the resultant approach.

TPLBLS remarkably enhanced the segmentation results of both cases: First, single target segmentation (one heart ventricle and meningioma brain tumor) according to Table 1 and Table 3 respectively. Second, two targets simultaneous segmentation represented in table 4. For left ventricle endocardium segmentation, the DC increases to 95.74%, the RMSE is reduced to 0.023 and the MHD is 0.059. According to the RMSE and MHD metrics, these results are still satisfactory, and even better evaluated when considering only part of the image (66x71) including the ROI. For right ventricle endocardium segmentation, the DC is 86%, the RMSE is about 0.093 and the MHD 0.48. For meningioma brain tumor extraction results, the DC becomes 90.98%, the RMSE is reduced to half (0.049) and the MHD takes even less (about 0.31). TPLBLS also enhanced the biventricular segmentation; DC 87.67%, MHD 1.45

and RMSE 0.24. These improvements are caused by the fact that the topology of the evolving contour is better controlled and preserved by TPLBLS model rather than LBLS. It has been shown that the TPLBLS can also be a promising approach for the simultaneous segmentation of different objects such as both ventricles of the heart as in [24] as long as the process is initiated with the proper number of initial contours. This strongly qualifies our TPSBLS to be suitable for an even larger field of exploitation that concerns simultaneous multi-targets segmentations.

Since both of our approaches, SBLS and TPSBLS, can be applied directly and do not require any training phase it was possible to obtain segmentation results even for a small number of slices, unlike ATLAS based [3], [4] and U-NET [7], [8] techniques where the user must select a large number of representative slices for the training phase, otherwise the model will not be suitable for each element (slice) of the validation or the test data. In this case, it may fail to correctly segment the target. A further advantage of our approach is that the user can easily choose to simultaneously segment more than just one object simply by setting as many initial contours as desired targets. For both LBLS and TPLBLS and for the best possible segmentation results, the initial contour needs to be near to the target. On the other hand, it is true that our method requires setting two parameters manually: α the constant velocity term of φ and μ the positive tuning parameter, which seems to be a limitation of our system. The model can provide results using fixed values of α and μ but the quality will be poor.

As future work, TPSBLS model can be improved to be less operator-dependent, providing a model which doesn't require setting parameters, less sensitive to the initial contour location and more suitable for the segmentation of other substances such as brain tumors and for other kinds of medical imaging such as X-rays and Computed Tomography. Due to its properties TPSBLS helps to open new research directions; it can be used to segment multi-targets simultaneously such as both lung boundaries identification on CT images and any other multi-

targets simultaneous segmentation like blood cells. We should also consider, as a future step of our work, improving our proposed deformable model to achieve 3D volume segmentation.

References

[1] L. Lucchese, S. K. Mitra, and S. Barbara, “Color Image Segmentation: A State-of-the-Art Survey,” *Proc. Indian Natl. Sci. Acad.*, vol. 67, no. 2A, 2015.

[2] D. L. Pham, C. Xu, and J. L. Prince, “Current methods in medical image segmentation,” *Annu. Rev. Biomed. Eng.*, vol. 2, pp. 315–337, 2000.

[3] Y. Ou et al, “Multi-Atlas Segmentation of the Cardiac MR Right Ventricle,” in *Proceedings of 3D Cardiovascular Imaging: A MICCAI Segmentation Challenge*, pp. 1–6, 2012.

[4] L. Sun, L. Zhang, and D. Zhang, “Multi-Atlas Based Methods in Brain MR Image Segmentation,” *Chinese Med. Sci. J.*, vol. 34, no. 2, pp. 110–119, 2019.

[5] E. M. Van Rikxoort *et al.*, “Adaptive local multi-atlas segmentation : Application to the heart and the caudate nucleus,” *Med. Image Anal.*, vol. 14, no. 1, pp. 39–49, 2010.

[6] M. Lorenzo-valdés et al, “Segmentation of 4D cardiac MR images using a probabilistic atlas and the EM algorithm,” *Med. Image Anal.*, vol. 8, pp. 255–265, 2004.

[7] O. Ronneberger, P. Fischer, and T. Brox, “U-Net : Convolutional Networks for Biomedical Image Segmentation,” in *International Conference on Medical Image Computing and Computer-Assisted Intervention*, 2015, pp. 234–241.

[8] Y. He et al, “A 3D Dual Path U-Net of Cancer Segmentation Based on MRI,” in *IEEE 3rd International Conference on Image, Vision and Computing (ICIVC)*, 2018, pp. 268–272.

[9] D. Grosgeorge et al, “Graph cut segmentation with a statistical shape model in cardiac MRI,” *Comput. Vis. Image Underst.*, vol. 117, no. 9, pp. 1027–1035, 2013.

[10] L. He *et al.*, “A comparative study of deformable contour methods on medical image segmentation,” *Image Vis. Comput.*, vol. 26, pp. 141–163, 2008.

[11] T. Heimann and H. P. Meinzer, “Statistical shape models for 3D medical image segmentation: A review,” *Med. Image Anal.*, vol. 13, no. 4, pp. 543–563, 2009.

[12] L. D.Cohen, “On active contour models and balloons,” *CVGIP Image Underst.*, vol. 53, no. 2, pp. 211–218, 1991.

[13] T. F. Cootes et al, “Active Shape Models-Their Training and Application,” *Comput. Vis. Image Underst.*, vol. 61, no. 1, pp. 38–59, 1995.

[14] C. Xu and J. L. Prince, “Snakes , Shapes , and Gradient Vector Flow,” *IEEE Trans. Image Process.*, vol. 7, no. 3, pp. 359–369, 1998.

[15] R. Malladi, J. A. Sethian, and B. C. Vemuri, “Shape Modeling with Front Propagation : A Level Set Approach,” *IEEE Trans. Pattern Anal. Mach. Intell.*, vol. 17, no. 2, pp. 158–175, 1995.

[16] J. A. Sethian, “LEVEL SET METHODS AND FAST MARCHING METHODS: EVOLVING INTERFACES IN COMPUTATIONAL GEOMETRY, FLUID MECHANICS, COMPUTER VISION, AND MATERIALS SCIENCE,” *Robotica*, vol. 18, pp. 89–92, 2000.

[17] H. Khotanlou, O. Colliot, and I. Bloch, “Automatic Brain Tumor Segmentation Using Symmetry Analysis and Deformable Models,” *Adv. Pattern Recognit.*, pp. 198–202, 2006.

[18] H. Khotanlou et al, “3D brain tumor segmentation in MRI using fuzzy classification , symmetry analysis and spatially constrained deformable models,” *Fuzzy Sets Syst.*, vol. 160, pp. 1457–1473, 2009.

[19] S. S. Babu et al, “The parametric deformable model for image detection of brain tumors,” *Int. J. Pure Appl. Math.*, vol. 115, no. 6, pp. 171–175, 2017.

[20] M. R. Avendi, A. Kheradvar, and H. Jafarkhani, “Automatic Segmentation of the Right Ventricle from Cardiac MRI Using a Learning-Based Approach,” *Magn. Reson. Med.*, vol. 78, no. 6, pp. 2439–2448, 2017.

[21] M. R. Avendi, A. Kheradvar, and H. Jafarkhani, “A Combined Deep-Learning and Deformable-Model Approach to Fully Automatic Segmentation of the Left Ventricle in Cardiac MRI,” *Med. Image Anal.*, vol. 30, pp. 108–119, 2016.

[22] C. M. S. Nambakhsh et al, “Right ventricle segmentation with probability product kernel constraints,” *Lect. Notes Comput. Sci. (including Subser. Lect. Notes Artif. Intell. Lect. Notes Bioinformatics)*, pp. 509–517, 2013.

[23] A. Bhan, “Parametric Models for Segmentation of Cardiac MRI database with Geometrical Interpretation,” *Int. Conf. Signal Process. Integr. Networks (SPIN), Noida, India*, no. 2, pp. 711–715, 2014.

[24] C. Arrieta *et al.*, “Biomedical Signal Processing and Control Simultaneous left and right ventricle segmentation using topology preserving level sets,” *Biomed. Signal Process. Control*, vol. 33, pp. 88–95, 2017.

[25] A. Montillo, D. Metaxas, and L. Axel, “Automated Model-Based Segmentation of the Left and Right Ventricles in Tagged Cardiac MRI,” *Med. Image Comput. Comput. Interv. - MICCAI 2003*, pp. 507–515, 2003.

[26] S. Soomro et al, “Segmentation of Left and Right Ventricles in Cardiac MRI Using Active Contours,” *Comput. Math. Methods Med.*, vol. 2017, pp. 1–16, 2017.

[27] X. Han, C. Xu, and J. L. Prince, “A topology preserving level set method for geometric

deformable models," *IEEE Trans. Pattern Anal. Mach. Intell.*, vol. 25, pp. 755–768, 2003.

[28] V. Caselles, R. Kimmel, and G. Sapiro, "Geodesic Active Contours," *Int. J. Comput. Vis.*, vol. 22, pp. 61–79, 1997.

[29] S. Kichenassamy et al, "Conformal curvature flows: From phase transitions to active vision," *Arch. Ration. Mech. Anal.*, vol. 134, no. 3, pp. 275–301, 1996.

[30] N. Forcadel and C. Le Guyader, "A short time existence / uniqueness result for a nonlocal topology-preserving segmentation model," *J. Differ. Equ.*, vol. 253, no. 3, pp. 977–995, 2012.

[31] T. F. Chan and L. A. Vese, "Active Contours Without Edges," *IEEE Trans. Image Process.*, vol. 10, no. 2, pp. 266–277, 2001.

[32] J. Duan, Z. Pan, X. Yin, W. Wei, and G. Wang, "Some fast projection methods based on Chan-Vese model for image segmentation," *Duan al. EURASIP J. Image Video Process.*, pp. 1–16, 2014.

[33] A. Almhdie *et al.*, "Chan-Vese based method to segment mouse brain MRI images : application to cerebral malformation analysis in trisomy 21 To cite this version : HAL Id : hal-00608092," in *2009 17th European Signal Processing Conference*, 2011, pp. 1883–1887.

[34] X. Hu et al, "Topology-aware segmentation using descrite morse theory," in *ICLR*, pp. 1–19, 2021.

[35] S. Vasu, M. Kozinski, L. Citraro, and P. Fua, "TopoAL: An Adversarial Learning Approach for Topology-Aware Road Segmentation," *Lect. Notes Comput. Sci. (including Subser. Lect. Notes Artif. Intell. Lect. Notes Bioinformatics)*, vol. 12372 LNCS, pp. 224–240, 2020.

[36] Q. Ge et al, "Enhancing the morphological segmentation of microscopic fossils through Localized Topology-Aware Edge Detection," *Auton. Robots*, pp. 1–16, 2020.

[37] S. Y. Shin et al, "Deep Small Bowel Segmentation with Cylindrical Topological Constraints," *Lect. Notes Comput. Sci. (including Subser. Lect. Notes Artif. Intell. Lect. Notes Bioinformatics)*, vol. 12264, pp. 207–215, 2020.

[38] S. Shit et al, "clDice - a Novel Topology-Preserving Loss Function for Tubular Structure Segmentation," *Comput. Vis. Pattern Recognit.*, pp. 1–11, 2020.

[39] Y. Bai et al, "Topology-preserving Geometric Deformable Model on Adaptive Quadtree Grid," in *IEEE Conference on Computer Vision and Pattern Recognition, Minneapolis, MN, USA*, pp. 1–8, 2007.

[40] F. Ségonne, "Active Contours Under Topology Control — Genus Preserving," pp. 107–117, 2008.

[41] C. Le Guyader and L. A. Vese, “Self-Repelling Snakes for Topology-Preserving Segmentation Models,” in *IEEE Transactions on Image Processing*, vol. 17, no. 5, pp. 767–779, 2008.

[42] H. Schaeffer et al, “Topology preserving active contours,” *Commun. Math. Sci.*, vol. 12, no. 7, pp. 1329–1342, 2014.

[43] N. Duggan, “Topology Preserving and Robust Variational Image Segmentation Models with Applications in Medical Imaging,” PhD thesis, National University of Ireland, Galway, 2015.

[44] K. Zhang et al, “Active contours with selective local or global segmentation : A new formulation and level set method,” *Image Vis. Comput.*, vol. 28, no. 4, pp. 668–676, 2010.

[45] Y. Yahia Lahssene, L. Meddeber, T. Zouagui, and R. Jennane, “A topology constrained geometric deformable model for medical image segmentation,” *Biomed. Signal Process. Control*, vol. 64, no. January 2020, p. 102299, 2021.

[46] A. Budai et al, “Computerized Medical Imaging and Graphics Fully automatic segmentation of right and left ventricle on short-axis cardiac MRI images,” *Comput. Med. Imaging Graph.*, vol. 85, pp. 1–9, 2020.

[47] C. Petitjean, “MR images and contour data,” 2012. [Online]. Available: http://pagesperso.litislab.fr/cpetitjean/mr-images-and-contour-data/. [Accessed: 18-Jan-2023].

[48] A. Andreopoulos and J. K. Tsotsos, “Efficient and generalizable statistical models of shape and appearance for analysis of cardiac MRI,” *Med. Image Anal.*, vol. 12, no. 3, pp. 335–357, 2008.

[49] O. Bernard *et al.*, “Deep Learning Techniques for Automatic MRI Cardiac Multi-Structures Segmentation and Diagnosis: Is the Problem Solved?,” *IEEE Trans. Med. Imaging*, vol. 37, no. 11, pp. 2514–2525, 2018.

[50] C. Jun, “Brain tumor dataset. figshare. Dataset.,” 2017. [Online]. Available: https://doi.org/10.6084/m9.figshare.1512427.v5. [Accessed: 18-Jan-2023].

[51] R. W. Chan et al, “Magnetic Resonance Imaging,” *Encycl. Biomed. Eng. Elsevier*, pp. 574–587, 2019.

[52] J. O. S. H. Cleary and A. R. Guimarães, “Magnetic Resonance Imaging,” *Pathobiol. Hum. Dis. A Dyn. Encycl. Dis. Mech.*, pp. 3987–4004, 2014.

[53] F. W. Wehrli, “Progress in Nuclear Magnetic Resonance Spectroscopy,” *From NMR Diffr. zeugmatography to Mod. imaging beyond*, pp. 87–135, 1995.

[54] J. A. Detre, “Magnetic resonance imaging.,” *Br. J. Theatre Nurs.*, vol. 1, no. 3, pp. 793–800, 1991.

[55] Eric T. Chou and John A. Carrino, “Magnetic Resonance Imaging,” *Pain Manag.*, pp. 106–117, 2007.

[56] D. C. Lee and T. J. Carroll, “Magnetic resonance imaging,” in *Imaging of Pain*, R. S. D. C. Steven D. Waldman, Ed. pp. 251–273, 2010.

[57] M. BAGHDADI, “Contribution à l ’ Analyse et à la Segmentation d ’ Images Médicales 3D,” PhD thesis, University of sciences and technology Mohamed Boudiaf. Oran. Algérie, 2019.

[58] T. B. Smith and K. S. Nayak, “MRI artifacts and correction strategies,” *Imaging Med.*, vol. 2 (4), pp. 445–457, 2010.

[59] C. A. Cocosco et al, “BrainWeb: online interface to a 3D MRI simulated brain database,” *Neuroimage*, vol. 5, no. 4, 1997.

[60] Y. He, X. Yu, C. Liu, J. Zhang, K. Hu, and H. C. Zhu, “A 3D Dual Path U-Net of Cancer Segmentation Based on MRI,” in *3rd IEEE International Conference on Image, Vision and Computing*, 2018, pp. 268–272.

[61] S. L. Thornton, “Snakes,” *Encycl. Toxicol. Third Ed.*, vol. 331, pp. 310–312, 2014.

[62] L. D. Cohen, “Appeared drst as RR INRIA 1075,” *Comput. Vision, Graph. Image Process. Image Underst.*, vol. 53, no. 2, pp. 211–218, 1991.

[63] C. Chesnaud, P. Rélrégier, and V. Boulet, “Statistical region snake-based segmentation adapted to different physical noise models,” *IEEE Trans. Pattern Anal. Mach. Intell.*, vol. 21, no. 11, pp. 1145–1157, 1999.

[64] T. McInerney and T. Demetri, “Deformable Models in Medical Image Analysis : A Survey,” *Med. Image Anal.*, vol. 1, no. 2, pp. 91–108, 1996.

[65] V. Caselles et al, “A geometric model for active contours in image processing,” *Numer. Math.*, vol. 66, no. 1, pp. 1–31, 1993.

[66] R. Goldenberg et al, “Fast geodesic active contours,” *Lect. Notes Comput. Sci. (including Subser. Lect. Notes Artif. Intell. Lect. Notes Bioinformatics)*, vol. 1682, no. 1, pp. 34–45, 1999.

[67] V. Caselles et al, “Minimal surfaces based object segmentation,” *IEEE Trans. Pattern Anal. Mach. Intell.*, vol. 19, no. 4, pp. 394–398, 1997.

[68] S. Kichenassamy et al, “Gradient flows and geometric active contour models,” *IEEE Int. Conf. Comput. Vis.*, pp. 810–815, 1995.

[69] A. Yezzi et al, “A geometric snake model for segmentation of medical imagery,” *IEEE Trans. Med. Imaging*, vol. 16, no. 2, pp. 199–209, 1997.

[70] K. Siddiqi et al, “Area and length minimizing flows for shape segmentation,” *IEEE*

Trans. Image Process., vol. 7, no. 3, pp. 433–443, 1998.

[71] A. Yezzi, J. Andy, and T. Alan, "A Statistical Approach to Snakes for Bimodal and Trimodal Imagery," in *Proceedings of the Seventh IEEE International Conference on Computer Vision.*, 1999.

[72] N. Paragios and R. Deriche, "Geodesic Active Contours and Level Sets for the Detection and Tracking of Moving Objects," *Pattern Anal. Mach. Intell. IEEE Trans.*, vol. 22, no. 3, pp. 266–280, 2004.

[73] M. E. Leventon, W. E. L. Grimson, and O. Faugeras, "Statistical shape influence in geodesic active contours," *Biomed. Imaging V - Proc. 5th IEEE EMBS Int. Summer Sch. Biomed. Imaging, SSBI*, pp. 1–8, 2002.

[74] Y. Y. Boykov and M. P. Jolly, "Interactive graph cuts for optimal boundary & region segmentation of objects in N-D images," *Proc. IEEE Int. Conf. Comput. Vis.*, vol. 1, pp. 105–112, 2001.

[75] B. B. Kimia, A. R. Tannenbaum, and S. W. Zucker, "Shapes, Shocks, and Deformations h The Components of Two-Dimensional Shape and the Reaction-Diffusion Space," *Int. J. Comput. Vis.*, vol. 15, pp. 189–224, 1995.

[76] S. Osher, "Fronts Propagating with Curvature- Dependent Speed : Algorithms Based on Hamilton-Jacobi Formulations," *J. Comput. Phys.*, vol. 49, pp. 12–49, 1988.

[77] J. A. Sethian, "A fast marching level set method for monotonically advancing fronts," *Proc. Natl. Acad. Sci. USA*, vol. 93, pp. 1591–1595, 1996.

[78] P. H. J. Keener *et al.*, *"Level Set Methods and Dynamic Implicit Surfaces,"* vol. 153. 2003.

[79] J. a. Sethian, "Level set methods and fast marching methods: Evolving interfaces in computational geometry, fluid mechanics, computer vision, and materials science," *Cambridge Univ. Press*, 1999.

[80] H. Delingette and J. Montagnat, "New Algorithms for Controlling Active Contours Shape and Topology," in *European Conference on Computer Vision*, pp. 381–395, 2000.

[81] N. Paragios, "Geodesic Active Regions : A New Framework to Deal with Frame Partition Problems in Computer Vision 1," *J. Vis. Commun. Image Represent.*, vol. 13, pp. 249–268, 2002.

[82] W. Fang and K. L. Chan, "Incorporating shape prior into geodesic active contours for detecting partially occluded object," *Pattern Recognit.*, vol. 40, pp. 2163–2172, 2007.

[83] D. B. Mumford and S. Jayant, "Optimal Approximations by Piecewise Smooth Functions and Associated Variational Problems," *Commun. Pure Appl. Math.*, vol. XLII, pp. 577–685, 1989.

[84] Y. N. Law, H. K. Lee, and A. M. Yip, "A Multiresolution Stochastic Level Set Method for Mumford – Shah Image Segmentation," *IEEE Trans. IMAGE Process.*, vol. 17, no. 12, pp. 2289–2300, 2008.

[85] A. Almhdie *et al.*, "Chan-vese based method to segment mouse brain mri images: Application to cerebral malformation analysis in Trisomy 21," *Eur. Signal Process. Conf.*, pp. 1883–1887, 2009.

[86] J. Dong and C. Hao, "3D fast level set image segmentation based on Chan-Vese model," *3rd Int. Conf. Bioinforma. Biomed. Eng. iCBBE*, pp. 9–12, 2009.

[87] J. W. Craggs, "Applied Mathematical Sciences," *Math. Gaz.*, vol. 57, no. 399, 1973.

[88] L. A. Vese and T. F. Chan, "A Multiphase Level Set Framework for Image Segmentation Using the Mumford and Shah Model," *Int. J. Comput. Vis.*, vol. 50, no. 3, pp. 271–293, 2002.

[89] C. Li et al, "Implicit active contours driven by local binary fitting energy," *Proc. IEEE Comput. Soc. Conf. Comput. Vis. Pattern Recognit.*, 2007.

[90] C. Li et al, "Minimization of region-scalable fitting energy for image segmentation," *IEEE Trans. Image Process.*, vol. 17, no. 10, pp. 1940–1949, 2008.

[91] C. Li et al, "Level set evolution without re-initialization: A new variational formulation," *Proc. - IEEE Comput. Soc. Conf. Comput. Vis. Pattern Recognition, CVPR*, vol. I, pp. 430–436, 2005.

[92] P. Bazin, L. M. Ellingsen, and D. L. Pham, "Digital Homeomorphisms in Deformable Registration," in *Karssemeijer N., Lelieveldt B. (eds) Information Processing in Medical Imaging. IPMI*, pp. 211–222, 2007.

[93] M. Möller et al, "A framework for automated cell tracking in phase contrast microscopic videos based on normal velocities," *J. Vis. Commun. Image R.*, vol. 25, pp. 396–409, 2014.

[94] X. Han et al, "Topology Correction in Brain Cortex Segmentation Using a Multiscale , Graph-Based Algorithm," *IEEE Trans. Med. Imaging*, vol. 21, no. 2, pp. 109–121, 2002.

[95] G. Bertrand, "Simple points, topological numbers and geodesic neighborhoods in cubic grids," *Pattern Recognit. Lett.*, vol. 15, pp. 1003–1011, 1994.

[96] Y. Bai, X. Han, and J. L. Prince, "Octree Grid Topology Preserving Geometric Deformable Model for Three-Dimensional Medical Image Segmentation," *Inf. Process. Med. Imaging*, vol. 4584, pp. 556–568, 2007.

[97] B. Fischl, A. Liu, and A. M. Dale, "Automated Manifold Surgery : Constructing Geometrically Accurate and Topologically Correct Models of the Human Cerebral Cortex," *IEEE Trans. Med. Imaging*, vol. 20, no. 1, pp. 70–80, 2001.

[98] I. Guskov and Z. J. Wood, “Topological Noise Removal,” in *Graphics Interface Proceedings: Ottawa, Canada,* pp. 19–26, 2001.

[99] N. Kriegeskorte and R. Goebel, “An Efficient Algorithm for Topologically Correct Segmentation of the Cortical Sheet in Anatomical MR Volumes,” *Neuroimage*, vol. 14, pp. 329–346, 2001.

[100] D. W. Shattuck and R. M. Leahy, “Automated Graph-Based Analysis and Correction of Cortical Volume Topology,” *IEEE Trans. Med. Imaging*, vol. 20, no. 11, pp. 1167–1177, 2001.

[101] F. Ségonne, “Segmentation of Medical Images under Topological Constraints,” PhD thesis, Massachusetts Institute of technology, 2005.

[102] S. Florent et al, “A novel level set framework for the segmentation of medical images under topology control,” *MIT-CSAIL-TR-2005-038, Massachusetts Inst. Technol. Cambridge, ma 02139 USA*, pp. 1–17, 2005.

[103] F. Ségonne, “Active Contours Under Topology Control — Genus Preserving,” *Int J Comput Vis*, vol. 79, pp. 107–117, 2008.

[104] C. Hsu, C. Yang, and H. Wang, “Topological control of level set method depending on topology constraints,” *Pattern Recognit. Lett.*, vol. 29, pp. 537–546, 2008.

[105] S. Gupta, N. S. Punn, and S. K. Sonbhadra, “MAG-Net: Mutli-task attention guided network for brain tumor segmentation and classification,” *eess.IV*, pp. 1–13, 2021.

[106] A. Rehman et al, “Deep AutoEncoder-Decoder Framework for Semantic Segmentation of Brain Tumor,” *Aust. J. Intell. Inf. Process. Syst.*, vol. 15, no. 4, pp. 54–60, 2019.

[107] E. Yörük, E. Konuko, and B. Sankur, “Shape-Based Hand Recognition,” *IEEE Trans. Image Process.*, vol. 15, no. 7, pp. 1803–1815, 2006.

[108] N. Singh, S. Pawar, and Y. K. Jain, “Efficient Face Detection Method using Modified Hausdorff Distance Method with C4.5 Classifier and Canny Edge Detection,” *Int. J. Comput. Appl.*, vol. 123, no. 10, pp. 38–44, 2015.

[109] A. Pujol and J. L. Alba-castro, “A Supervised Modification of The Hausdorff Distance for Visual Shape Classification,” *Int. J. Pattern Recognit. Artif. Intell.*, vol. 123, 2011.

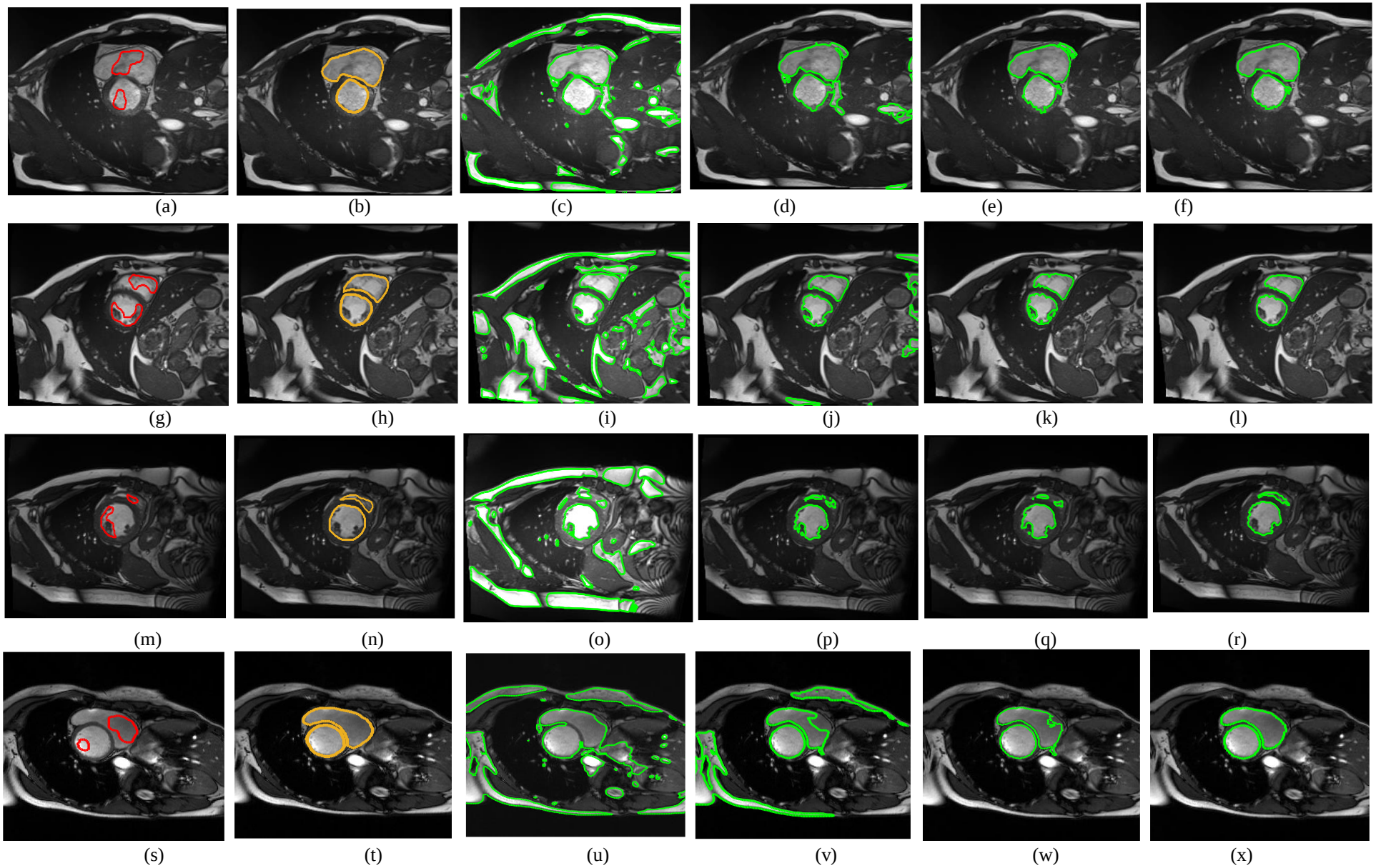

Fig. 5. 14. Simultaneous left and right ventricle segmentation results of CV, LBGFRLS, LBLS and TPLBLS. Images with initial contour (a), (g), (m) and (s) - heart image from MICCAI 2017. GT (b), (h), (n) and (t). CV segmentation results (c), (i), (o) and (u). LBGFRLS segmentation results (d), (j), (p) and (v). LBLS segmentation results (e), (k), (q) and (w). TPLBLS segmentation results (f), (l), (r) and (x). (c) DC= 3.1760 , (d) DC= 82.5265 , (e) DC= 94.6113, (f) μ=12, DC= 96.3986 , (i) DC= 6.9859, (j)) DC= 42.3077, (k) DC= 62.9482, (l) μ= 12, DC= 84.8168, (o) DC= 5.8365, (p)) DC= 80.0149, (q) DC= 81.5413, (r) μ= 8, DC= 88.0250, (u) DC= 1.5775 , (v)) DC= 54.4517, (w) DC= 94.9314 , (x) μ=5, DC= 97.1878. Initial contours are in red. Ground truths are in orange. Obtained contours are in green.